

MINIMIZATION OF THE RF LINK LOSS OF A NEUROPOTENTIAL RECORDING SYSTEM USING METAMATERIAL BASED ANTENNAS

A thesis submitted to
the Department of Electrical & Electronic Engineering
of
Bangladesh University of Engineering & Technology
in partial fulfillment of the requirements for the degree of
**Master of Science in
Electrical & Electronic Engineering**

by

M. Shifatul Islam: 1018062211



Department of Electrical & Electronic Engineering
Bangladesh University of Engineering and Technology (BUET)

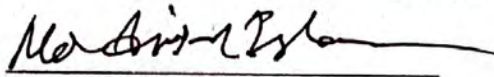
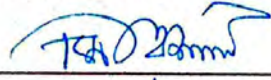
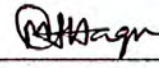
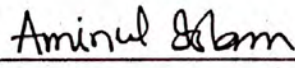
Dhaka-1000, Bangladesh

November 2021

Certification

The thesis titled "MINIMIZATION OF THE RF LINK LOSS OF A NEUROPOTENTIAL RECORDING SYSTEM USING METAMATERIAL BASED ANTENNAS" submitted by M. Shifatul Islam, Roll No.: 1018062211, Session: October 2018, has been accepted as satisfactory in partial fulfillment of the requirement for the degree of Master of Science in Electrical and Electronic Engineering on ^{dit} ~~September 26,~~ ^{November 24,} 2021.

BOARD OF EXAMINERS

1. 
Dr. Md. Asiful Islam
Associate Professor
Department of EEE, BUET, Dhaka
Chairman
(Supervisor)
2. 
Dr. Md. Kamrul Hasan
Professor and Head
Department of EEE, BUET, Dhaka
Member
(Ex- officio)
3. 
Dr. Mohammad Ariful Haque
Professor
Department of EEE, BUET, Dhaka
Member
4. 
Major Md Aminul Islam, PhD
Assistant Professor
Department of EECE, MIST, Dhaka
Member
(External)

Declaration

I hereby declare that this thesis has been an independent and individual one, any part of which has not been submitted elsewhere as a previous work for any degree before.

Signature of the Candidate

M. Shifatul Islam

M. Shifatul Islam

Student ID: 1018062211

Table of Contents

Certification	ii
Declaration	iii
Table of Contents	iv
List of Figures	viii
List of Tables	xii
List of Symbols and Abbreviations	xiii
Acknowledgements	xv
Abstract	xvi
Chapter 1: Introduction	1
1.1 Motivation	1
1.2 Objectives	2
1.3 Thesis Outline	2
Chapter 2: Literature Study	4
2.1 Biopotential Sensing	4
2.1.1 Biopotentials	4

2.1.2	Active and Passive Sensing	6
2.2	Key Concepts for Gain Enhancement	10
2.2.1	Metamaterials	11
2.2.2	Resonant Cavities	15
2.3	Antenna Gain Enhancement Mechanisms	18
2.3.1	The LHM Inverse Focusing Technique	18
2.3.2	The Optical Lightening of the Source Medium	19
2.3.3	The Fabry Perot Resonator Cavity Concept	22
2.4	Possible Expectations in the Biosensing Application	30
 Chapter 3: Analysis of the Transmission Characteristics		32
3.1	Simulation Systems for Examining Transmission Enhancement	33
3.2	Transmission Analysis	41
3.3	Verification	43
3.4	Summary	45
 Chapter 4: Potential of the Proposed Concept in Biosensing		46
4.1	Designing of the Simulation Environment	46
4.2	Designing of the Antenna	49

4.3	Designing of the Superstrate and Metamaterial	50
4.4	Simulation	51
4.5	Performance Analysis	52
4.5.1	Transmission Characteristics	52
4.5.2	Misalignment Sensitivity	55
4.6	Comparison with a Closely Coupled Antenna Pair System	56
4.6.1	Design of the Antenna System	56
4.6.2	Transmission Analysis	57
4.7	Health Considerations	59
4.8	Biosensing at a Different Frequency	61
Chapter 5: A Passive Neurosensing System		63
5.1	System Design	63
5.2	Performance Analysis	64
5.2.1	Transmission Gain and Misalignment Sensitivity	64
5.2.2	SAR Calculation	65
5.3	System Level Modelling of Neuron Potential Extraction	66
5.3.1	System Overview	66
5.3.2	Resolution of the Spectrum	66

5.3.3 Simulation Results	67
Chapter 6: Conclusion	70
6.1 Major Contributions	70
6.2 Future Research Directions	70
References	72
Appendix A	A-1

List of Figures

Figure No.	Description	Page
2.1	The voltage and the frequency range of the common biopotential signals [5]	6
2.2	Realization of a neuropotential recording system over a layered head model [15]	8
2.3	Performance degradation of the antenna system presented in [16] with misalignment	10
2.4	The dielectric function of the periodic wire structure reported in [22], Fig. 2.4a is when we assume the wire is a perfect conductor, and Fig. 2.4b is when the wire is assumed to have a finite resistivity	12
2.5	Periodic rod structures capable of producing negative permittivity effects	13
2.6	The frequency dependent permeability function for the split ring resonators presented in [24]. Fig. 2.6a is the terminology of each variable mentioned in equations (2a) and (2b). Fig. 2.6b is the frequency dependent μ for ideal ring loops, and Fig. 2.6c is when the loops have a finite resistivity.	14
2.7	Geometric arrangement of an infinite resonant cavity [27]	16
2.8	The inverse focusing effect inside a DNG material, where the focused waves end up directing along the central horizontal axis	18
2.9	Wave incidence from a medium of lower refractive index than that of free space	19
2.10	Different metamaterial unit cells to induce optical lightning effect [32]	21

2.11	Gain enhancement of a source with a partially reflecting sheet above the ground	23
2.12	Practical realization of partially reflecting sheets to enhance transmission gain [33]	24
2.13	Simulations with single and multiple superstrates above an infinite ground plane, and the enhancement of directive gain [35]	26
2.14	Three different gain enhancement techniques on finite sized patch antenna. Fig. 2.14a is the use of stacked periodic structures to form LHM, Fig. 2.14b is the use of multiple superstrates, and Fig. 2.14c is the use of FSS imprints at the bottom of the superstrates.	28
2.15	Effect of superstrate reflection on the directive gain enhancement of finite sized antenna [37]. Fig. 2.15a is for the multiple superstrate configuration, Fig. 2.15b is for the FSS configuration	29
3.1	Geometric interpretation of the Fabry Perot resonator concept with the proposed idea. In Fig 3.1a, the waves leak away from the top and bottom sides, which is reflected inside to induce further reflection in Fig. 3.1b	33
3.2	Simplified antenna geometry for the analysis of the transmission performance in the simulation systems.	35
3.3	Step by step schematic diagram for the analysis of the two define antenna system. In Fig. 3.3a, the two antennas are separated without any engineering in between. In Fig. 3.3b the superstrate material is inserted between the two antennas. In Fig. 3.3c the air superstrate gap is filled with a material with dielectric constant of 2	37
3.4	The top view of the metamaterial imprinted superstrate and the unit cell. The reflectivity can be tuned by varying r, c, d	38
3.5	Effect of insulation coating to enhance transmission gain.	40
3.6	Effect of transmission enhancement with varying superstrate dielectric constant for system 1, Fig. 3.6a is the effect of superstrate inclusion, and Fig. 3.6b is the	41

	effect after the inclusion of gap material and circular rings.	
3.7	Effect of transmission enhancement with varying superstrate dielectric constant for system 2, Fig. 3.7a is the effect of superstrate inclusion, and Fig. 3.7b is the effect after the inclusion of gap material and circular rings.	42
3.8	Verification of Figs. 3.6a and 3.6b with CST Microwave Studio	44
3.9	Verification of Figs. 3.7a and 3.7b with CST Microwave Studio	44
4.1	Frequency dependent dispersive biological tissue with dielectric properties similar to ground beef	47
4.2	Convenient 3D and sectional view of the whole proof of concept simulation design. Fig. 4.2a is the geometry in HFSS, Figure 4.2b is the geometry in CST studio, and Figure 4.2c is the sectional view with the defining dimensions.	48
4.3	Geometry of the external (Fig. 4.3a) and the implant antenna (Fig. 4.3b) for the proof-of-concept design	49
4.4	Convergence plot of the simulation with increasing adaptive pass	51
4.5	Transmission loss for the proof-of-concept design	52
4.6	Performance degradation with misalignment along (a) x axis and (b) y axis	54
4.7	Sectional view of an antenna pair system without the engineering of the proposed concept.	57
4.8	Performance degradation of the close antenna pair system with misalignment along (a) x axis and (b) y axis	58
4.9	Cross sectional view of the SAR performance, averaged over 1g (Fig. 4.9a) and 10g (Fig. 4.9b) with input carrier power at 4.8 GHz set to 6 dBm (0.0039605 Watts)	60
4.10	Transmission performance of an antenna pair system designed at 2.4 GHz(HFSS)	61

5.1	Frequency dependent dielectric constant (ϵ) and conductivity (σ) of the tissues to design the neurosensing system.	63
5.2	Design of a passive neurosensing system with optimized transmission curves. [47]	64
5.3	Extraction of weak neuropotentials with the proposed antenna system.	67-69

List of Tables

Table No.	Description	Page
2.1	Voltage and frequency range of signals generated in human brain	9
3.1	Dimensions of the two antennas for each system, and for each step of the analysis. All units are in mm	39
4.1	Performance comparison of the proposed system with existing literature	53
4.2	Effect of misalignment in the transmission performance of the proposed design	55
4.3	Effect of misalignment in the transmission performance of the closely separated antenna pair	59
5.1	Effect of misalignment in the transmission performance of the neuropotential sensing system	65

List of Symbols and Abbreviations

DNG	Double NeGative
ECG	ElectroCardioGram
EEG	ElectroEncephaloGram
EMG	ElectroMyoGram
EOG	ElectroOculoGram
FEM	Finite Element Method
FIT	Finite Integration Technique
FSS	Frequency Selective Surface
LFP	Local Field Potential
LHM	Left Handed Material
MGP	Metamaterial Ground Planes
PEC	Perfect Electric Conductor
PMC	Perfect Magnetic Conduction
SAR	Specific Absorption Rate
SNR	Signal to Noise Ratio
TEM	Transverse Electro Magnetic
ϵ	Dielectric constant

μ	Relative permeability
σ	DC conductivity
$\tan\delta$	Loss tangent
ω_0	Resonant frequency of the metamaterial
ω_1	Secondary frequency for metamaterials

Acknowledgments

All praise to the almighty, who has kept me physically and mentally fit and granted me the mental strength to carry out such a detailed work. The whole research embarked on completely unexplored territory, and there were several experiments and simulation that have failed, and the journey was not easy. Praise to the almighty, who kept me strong in these days, to give me the resilience and the patience to see the work see the end.

The work was challenging, uncertain, but all the hard works seemed to pay off when the simulation results began to match with the expectations. I came across numerous fantastic works from great scientists and universities, which broadened my insights not just over the subject of antennas and biosensing, but over the whole domain of electromagnetism.

I thank my supervisor Dr. Md. Asiful Islam for continuously monitoring the work and providing me with valuable suggestions to overcome the constant difficulty I had been facing throughout the work. Even when things kept on going south, he kept patience with my work and over the whole time, we maintained a regular conversation again and again.

Special thanks to Prof. Dr. Asimina Kiourti, for sharing her valuable experience and wisdom to guide me over critical times. She corrected lots of my mistakes and provided a very helpful guidance to the overall development of the research.

Finally, I like to thank my parents, who kept bearing my misbehaves when I lost patience on the research and study, and always cheering, wishing me well over the whole endeavor.

Abstract

In this thesis, a novel method of performance enhancement for efficient biopotential sensing between antenna pairs has been presented, exploiting the concepts of superstrates and metamaterials. The superstrate and the antenna ground form a Fabry-Perot resonant cavity, and the inclusion of dielectric materials in-between the antenna patch and the superstrate are expected to enhance transmissions well as resulting in a miniaturized structure.

The ideas are tested on two simulation environments; first the two antennas are placed in free space, and later one antenna is buried inside a frequency dispersive tissue whose characteristics are like different biological tissues. For the case when the two antennas are buried in free space, a gain improvement of around $5dB$ is noted, when the two antennas are separated in free space, and when the antennas are separated by a biological medium, the improvement is found around $8dB$.

A proof-of-concept biosensing system with practical materials and frequency dispersive biological tissue is presented afterwards. For the design, the final transmission loss is found to be $-14.1 dB$ in HFSS, and $-12.33 dB$ in CST, both fair very well with the performance of the biosensing systems in the existing literature. However, the proposed concept also appears to be much less sensitive to misalignment between the two antennas, and the simulation results showed that the transmission degrade by less than $2.5 dB$, for 1 cm of misalignment. The safety measurements of specific absorption rate meet the desired requirements of patient safety and suggest that this method can be used for long term biosensing, and the proposed idea is also found to work in multiple frequencies.

Finally, a specific application of neuropotential has been addressed. An antenna pair system with practical human head materials is designed, which shows a transmission loss of $11.27 dB$ (HFSS) and $10.5 dB$ (CST) at a design frequency of $4.8 GHz$. And a demonstration of signal extraction has been presented. The novel idea can have significant contribution in the field of biosensing, although experimental data is still required for the practical discussions of the idea.

Chapter 1

Introduction

1.1 Motivation

Biopotentials, which are electrical signals generated from the electro-chemical activities of the biological cells, often provide significant information on the condition of a group of cells, or even broadly, the overall condition of any biological specimen. There are two types of biosensing methods which are currently the state of the art: the active sensing and the passive sensing. Most recently, the passive biosensing systems are growing in popularity as they lack the obtrusive circuitry, and easily wearable and portable. Passive sensing involves the communication between two antennas: an implant antenna which is used to transmit the weak biosignals and an external antenna, which captures the signal for the analysis of the external system. Current passive biosensing systems provide just about enough performance to extract the weakest biopotentials through an implant antenna, but this performance is susceptible to the misalignment of the antenna pairs, and therefore still not yet fully implementable over broad applications.

In the passive sensing systems, the two antennas are separated by a very small distance, and this makes overcoming the limitations a real challenge. On the other hand, a proper addressing of these limitations is required to make the passive biosensing systems feasible. For the pursuit of the solution to the problem, we explore a concept which has only been used in the far field communication enhancement between antenna pairs and is completely untested in the realm of interest.

The concept, which involves inserting superstrate material in front of the transmitting antenna has provided substantial directive gain enhancement for antennas in the far field. Being

motivated by the concept, we propose to enlarge the distance between the sensing antenna pairs and observe the transmission performance due to the insertion of similar dielectrics. The gap between the two antennas is enlarged just enough so that the far field approximation becomes just valid, and thus the Fabry Perot concept will hold for the antenna pairs as well.

1.2 Objectives

The main objectives of the thesis are:

- Design antenna pairs to operate at a frequency which has been used in passive sensing.
- Examine the effect of the Fabry Perot resonator antenna concept to enhance the transmission between the antenna pairs in the far field.
- Exploit the gap between the antenna pairs for further engineering to enhance performance
- Propose a proof-of-concept design for a passive biopotential sensing.
- Possible verification of the proof-of-concept design through suitable experiments.

1.3 Thesis Outline

In chapter 2, we shall discuss the existing literature on the passive biosensing systems, choose a baseline work as a benchmark for our research, and discuss the performance of the biosensing system presented there. We will also present the necessary theories and existing works of gain enhancement of the antennas in the far field, provide the theory of metamaterials and cavity resonators. We will end the section laying down the complete theoretical foundation, and the proposed novelty of the study with possible expectations.

In chapter 3, we will provide a rigorous simulation analysis to examine the transmission characteristics between two antennas separated by a particular distance, under variable conditions. We will examine the variation in the transmission performance with the change in the superstrate dielectric constant, with the inclusion of dielectric materials in between the external antenna and the superstrate and with the inclusion of circular ring imprints on both sides of the superstrate. Key conclusions will be drawn from the analysis, and we provide an estimation on

how much the proposed idea can enhance transmission between the antenna pairs, to highlight upon the potential in possible biosensing applications.

In chapter 4, we use the conclusions drawn in the previous section to design an antenna pair system with practical materials and biological sample tissue to simulate a biosensing system environment and compare the performance of the proposed proof of concept design with some of the existing works. We also provide an analysis on the misalignment sensitivity, and absorption measurements of the proposed biosensing system and end the section discussing the pros and cons of the proposed idea.

In chapter 5, we address a specific application of neuropotential sensing, design an antenna pair system on a layered system of human head and discuss the performance and applicability of the design in biosensing. We also present a full neurosignal extraction module to demonstrate a passive neuropotential sensing system.

Chapter 6 is the conclusion section, where we shall formally terminate the thesis with concluding remarks.

Chapter 2

Literature Study

In this section we provide the necessary background study to fully understand the problem which we are addressing in the research. The study was done in two sections:

- The study of biopotentials, biopotentials sensing mechanism, state of the art implementations and the limitations of the biosensing systems.
- The study of gain enhancement techniques for antennas in far field communication for efficient transmission.

Key concepts from the latter study will be applied to the former sensing systems to address the limitations and propose a high performance biopotential sensing design.

2.1 Biopotential Sensing

2.1.1 Biopotentials

Biopotentials are electric potentials which are generated from the volume conduction of currents generated from the electrochemical activities of a cluster of cells. Some of the most common biopotentials which can be monitored and extracted are:

- EEG (Electroencephalogram): EEG is the electric signals generated from the ionic currents generated within the neurons of human brain[1]. Diagnostic applications generally focus either on event-related potentials or on the spectral content of EEG. EEG is used to diagnose brain impairments such as sleep disorder, epilepsy, anesthesia, coma and even death.

- EMG (Electromyogram): EMG is the electric potential generated by muscle cells when these cells are electrically or neurologically activated [2]. EMG is used to diagnose different types of neuromuscular diseases.
- ECG (Electrocardiogram): ECG is a graph of voltage versus time of the electrical activity of the heart using electrodes placed on the skin[3]. These electrodes detect the small electrical changes that are a consequence of cardiac muscle depolarization followed by repolarization during each cardiac cycle (heartbeat). Changes in the normal ECG pattern occur in numerous cardiac abnormalities, including cardiac rhythm disturbances, inadequate coronary artery blood flow, and electrolyte disturbances.
- EOG (Electrooculogram): EOG is the corneo-retinal standing potential that exists between the front and the back of the human eye. The resulting signal is called the electrooculogram. Primary applications are in ophthalmological diagnosis and in recording eye movements[4].

In general, these biopotentials are extremely weak, with the magnitudes in the order of μV range, and the oscillation are maximum in the range of $\approx 100 Hz$ [5]. Fig. 2.1 shows the relative amplitude and the frequency range of the biopotentials.

Biosensing at such a low frequency is not a tractable choice since the scattering information will have very low resolution, but on the other hand, at high frequencies, the effect of tissue absorption also becomes prominent, and this reduces penetration. Therefore, the biosignals are often modulated with carriers at higher frequencies to provide sufficient resolution [6]. In [7], optimum frequencies for different dispersive biological tissues have been presented and it has been shown that the optimum frequency lies within the mid MHz to low GHz frequencies, and typically most biosensing systems operate at those elevated frequencies, instead of the fundamental frequency of the biopotentials themselves.

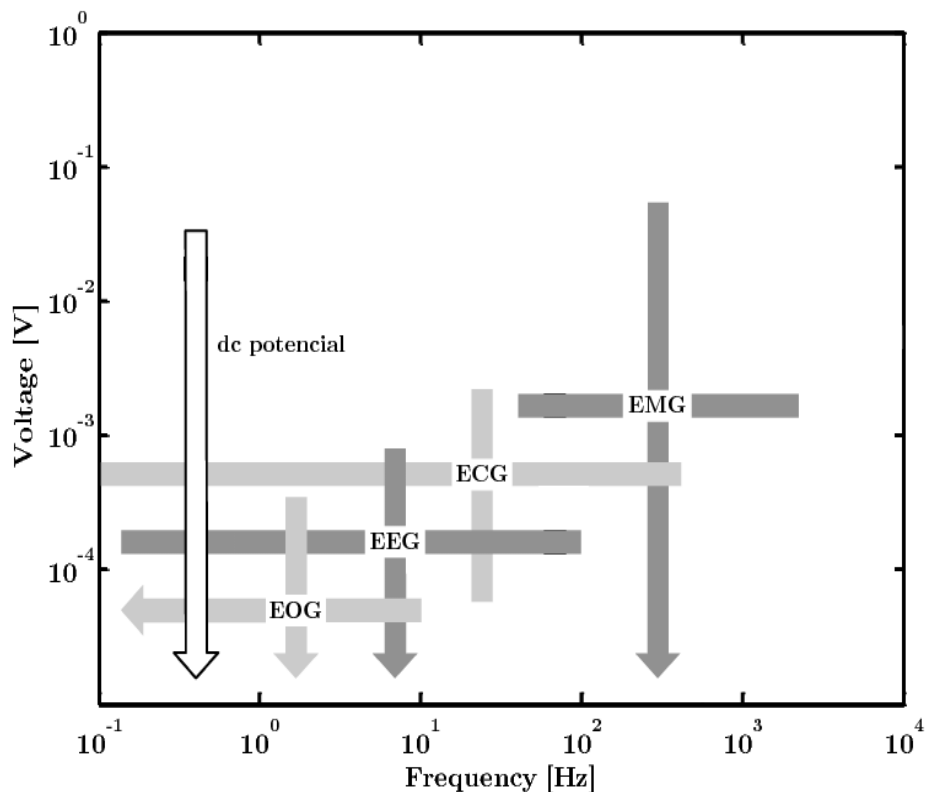


Figure 2.1: The voltage and the frequency range of the common biopotential signals [5]

2.1.2 Active and Passive Sensing

Biopotentials, such as neuropotentials modulate an externally generated carrier by means of nonlinear elements, such as varactors. The modulated carrier, conveying the internal neuropotential signal, is backscattered to an external detector that can demodulate and recover the original neuropotential signal. This backscattering is pervasive in RFID technology.

In the current state of the art literature, there are two different types of biosignals extraction techniques. The first one, we call the “active sensing”- where external circuitry is used to connect between the implant and the external antenna [8], and sometimes with the inclusion of batteries or energy harvesters [9,10]. The inclusion of circuitry makes the sensing system obtrusive and not so easily wearable, whereas the use of battery or energy harvesters may result

in heat generation inside the circuitry, which can disrupt normal brain operation. [11,12]. Almost all these recorded works were done on the neuropotentials (EEG brain signals), which demands the safety of the associated tissue cells even more.

Active sensing techniques with circuitry and harvesters are not a feasible method of long term and unobtrusive signal monitoring. Therefore, alternate solutions were sought in subsequent research. In [13] extensive use of batteries has been avoided to ensure more practical applicability, but there was still the need of using RF to dc converters, to power up the IC's, and therefore the risk of tissue damage still persists. As an alternative to the above methods, the first "fully passive" sensing systems were prescribed in [14,15].

A fully passive system does not need to regulate or rectify externally generated power in order to activate on-board circuitry. As a result, sophisticated and complex circuitry is completely excluded. Since the fully passive circuits dissipate little of the induced power, they have the potential to reduce risks associated with power dissipation in implants. However, in the fully passive case, the backscattering effect becomes of predominant interest since the fully passive device alone does not generate any RF signals. Its most notable success was demonstrated in the widely commercialized fully passive arterial pressure sensors, which have been implanted in over a hundred patients [14].

The design in [14] used microfabrication techniques to minimize footprint, maximize fabrication throughput, and minimize the number of off-chip components. The initial results were evaluated and potential feasibility as an implantable sensor has been tested through the results acquired from recording neuropotentials from frogs. The potential for ECoG and similar neurorecording applications were also discussed.

In [15], the authors reported the first use of microfabricated fully passive circuit for extracting and transmitting targeted neuropotentials wirelessly via the backscattering effect without any internal power source or harvester. Radiating electromagnetic waves experience attenuation, phase and wavelength alteration, and random scattering effects when propagating through dispersive biological media (i.e., human head), and these effects are augmented at microwave frequencies required for practical miniaturization of the integrated microsystem antenna. In the work, the implant antenna was buried inside a layered human head medium, and biosignals were extracted with the help of an "interrogator" (See Fig. 2.2)

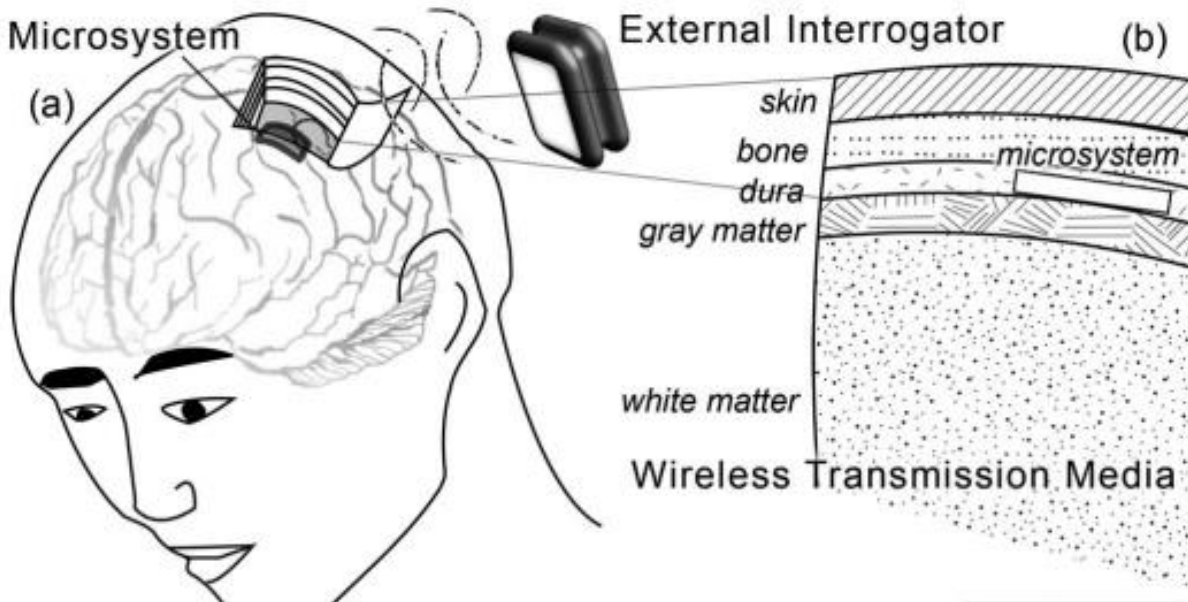


Figure 2.2: Realization of a neuropotential recording system over a layered head model [15]

These passive sensing systems are very attractive because of very minor heating issues and maintain a comfortable lifestyle. The transmission performance in those early works were improved in the further work [16], and the results were sufficient to extract the minimum neuropotential signals. The proposed system could detect brain signals as low as -82 dBm , which translates to a $50 \mu\text{V}$ brain signal. The weakest brain signals are in the range of $\approx 20 \mu\text{V}$ (See Table 1) and therefore there was still requirement for improvement.

In the subsequent work [17] the antenna dimensions were reduced, maintaining the similar amount of performance. In [18] another passive sensing system was proposed, which can detect brain signals as low as $\approx 63 \mu\text{V}$.

TABLE 2.1: VOLTAGE AND FREQUENCY RANGE OF SIGNALS GENERATED IN HUMAN BRAIN

NEURAL SIGNALS	VOLTAGE RANGE	FREQUENCY RANGE
ELECTROCORIOGRAPHIC SIGNALS	$100 - 200 \mu V_{pp}$	$< 500 Hz$
NEURAL SPIKES	$100 - 2000 \mu V_{pp}$	$300 Hz - 5 KHz$
LOCAL FIELD POTENTIALS (LFP)	$20 - 2000 \mu V_{pp}$	$< 500 Hz$

The work [16] served as the primary benchmark of the further works. In that work, the implant antenna was a modified patch antenna tuned to operate at two frequencies: $2.4 GHz$ and $4.8 GHz$. The external antenna was a spiral antenna, which has the characteristics to operate over a large frequency band without losing transmission performance. The external antenna communicates with the implant antenna at the lower frequency, and the implant antenna modulates the brain signals to transmit to the external antenna at the higher frequency, therefore the biosensing system was a dual band system. The transmission performance of the implant antenna at $4.8 GHz$ was reported to be $-19 dB$ ($-17 dB$ in simulation), which was sufficient enough to meet the requirements to extract the weakest brain signals. There was another interesting observation. The performance of the proposed passive sensing system was tested with the misalignment of the external antenna from the center position. The results show that for $1 cm$ of misalignment of the external antenna along the x and y axis result in loss increase of above $5 dB$, which is far from ideal, and the requirement for the passive sensing system to extract the weakest neuropotentials is not met. The performance degradation for the system with misalignment along both the axes is shown in Fig. 2.3.

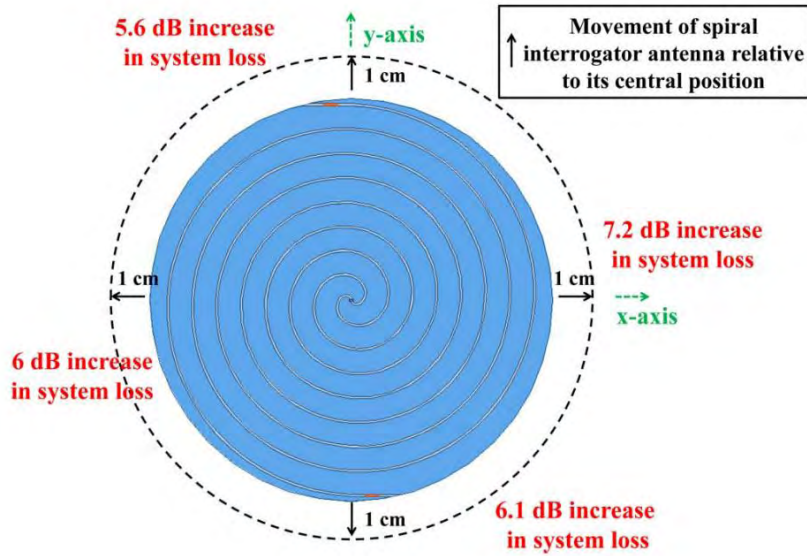


Figure 2.3: Performance degradation of the antenna system presented in [16] with misalignment

While the degradation of performance due to antenna offset is a major concern, there is little to do to address the problem. This is because, in passive sensing, the two antennas are inductively coupled to each other, and the separation between the two antennas is very small to engineering to boost transmission performance. This also leaves the scope of performance improvement of the passive sensors very limited. Most of the literature which has addressed biopotential sensing were only problem specific and addressing these limitations remains largely unaddressed to date.

2.2 Key Concepts for Gain Enhancement

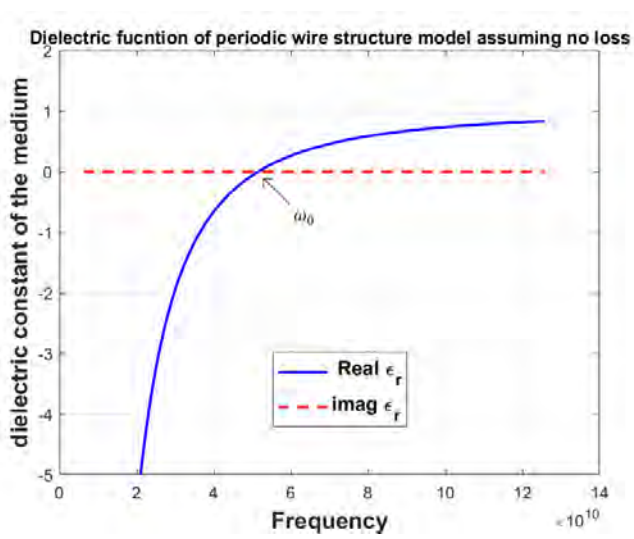
Since there is no existing work which deals with performance enhancement techniques of antenna pairs for such passive near field coupling, we shifted our attention to the general directive gain enhancement techniques which has been proposed to boost antenna transmission. Directive gain is a far field concept [19] which indicated the preferred direction where the

antenna radiation is maximum. The higher the directive gain of an antenna, the more the transmission along that direction and therefore the radiation is more efficient.

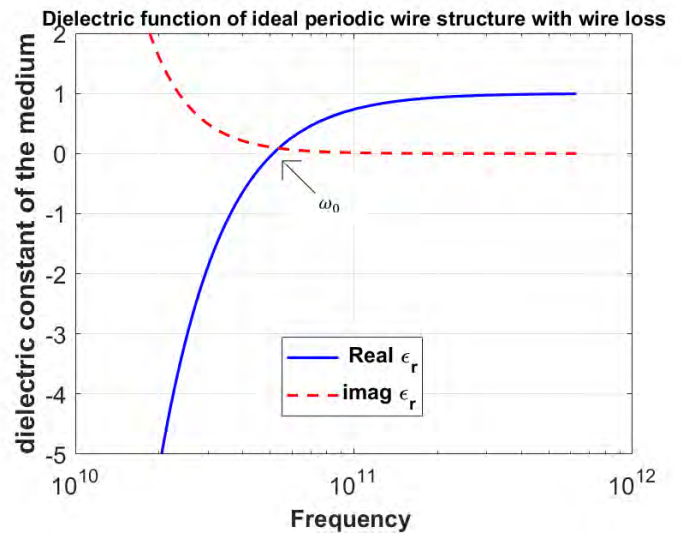
The most common way to attempt directivity enhancement is to modify the antenna structure, or to use antenna arrays. For biosensing systems, the use of antenna array is not feasible as it will take a lot of space. On the other hand, complex antenna structures have complex polarization, which is not desirable for near field coupling. Aside from modifying the antenna geometry, there are methods, which do not depend on the antennas structure but provides directivity enhancement. The methods which we have focused in our study have one thing in common: they all depend on the use of a “superstrate” material somewhere above the patch. By superstrate, we commonly refer to any additional dielectric slab at any distance above the radiating patch. In this section we discuss some of the engineering tools and terms which has been used to improve the directive gain of the antenna, while in the next section we will elaborate on the gain enhancement techniques with the presented tools:

2.2.1 Metamaterials

Metamaterials are artificial materials whose electromagnetic properties (dielectric constant ϵ and relative permeability μ) can be modified through external engineering. Long before the practical implementation of metamaterial, the idea was first laid down in [20], where he described the electromagnetic and optical phenomenon which a material with simultaneously negative ϵ and μ would provide. Although a superficial concept by that time, later, it has been shown that noble materials [21] do exhibit negative permittivity upto a certain frequency, which is dependent on the material structure itself. The work of [22,23] was first able to generate such negative ϵ effect over a periodic arrangement of rod structures. The negative permittivity effect was always seen below a particular given frequency, called the plasma resonant frequency ω_0 (See Fig. 2.4). The imaginary part, or the dielectric loss is ideally zero (See Fig. 2.4a), but for practically resistive material, this can acquire an abnormally large value at lower frequency (See Fig. 2.4b). The location of the plasma frequency for the rod structure can be adjusted with the following approximate equation [22]



(a)



(b)

Figure 2.4: The dielectric function of the periodic wire structure reported in [22], Fig. 2.4a is when we assume the wire is a perfect conductor, and Figure 2.4b is when the wire is assumed to have a finite resistivity

$$\omega_0 = \sqrt{\frac{2\pi c_0^2}{a^2 \ln\left(\frac{a}{r}\right)}} \dots \dots \dots (1)$$

Here C_0 is the speed of light in the vacuum, a is the separation between the rods, and r is the radius of the rod structure (See Fig. 2.5).

In a later work, [24] investigated periodic current loops and reported the presence of negative μ

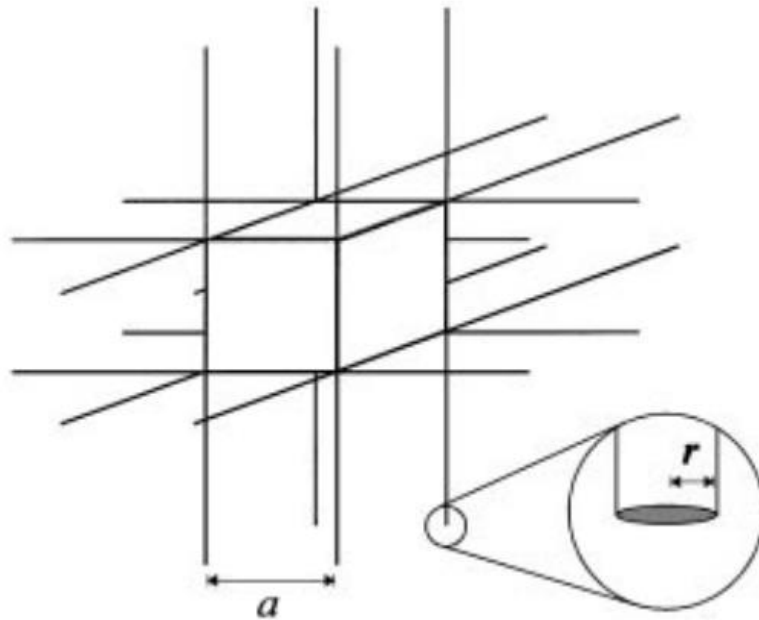
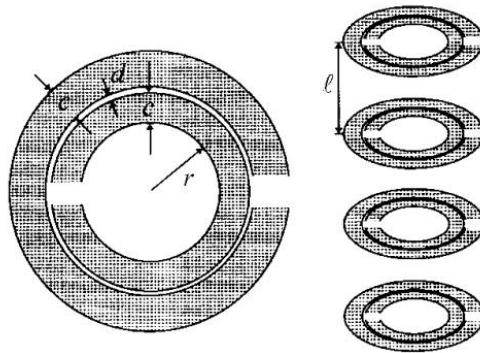


Figure 2.5: Periodic rod structures capable of producing negative permittivity effects [22]

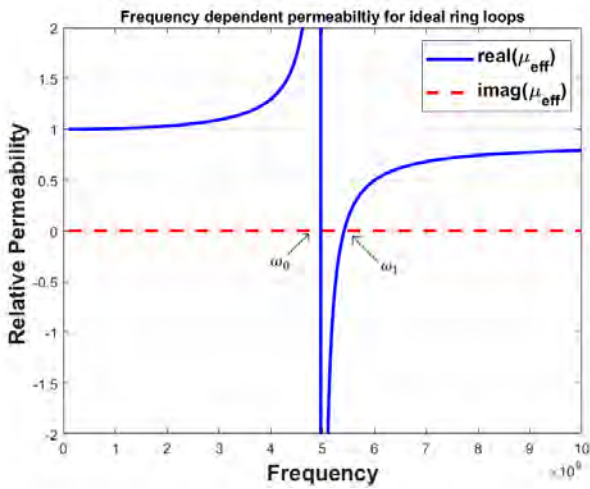
as well. The frequency dependent permeability function is different from what is shown in Fig. 2.4, and there are two frequencies of interest: the resonance frequency ω_0 and the secondary frequency ω_1 , within which the permeability is found to be negative only. For circular split rings, these two frequencies can be tuned to the desired value with the following equations:

$$\omega_0 = \sqrt{\frac{3lc_0^2}{\pi \ln\left(\frac{2c}{d}\right) r^3}} \quad \dots \dots \dots (2a)$$

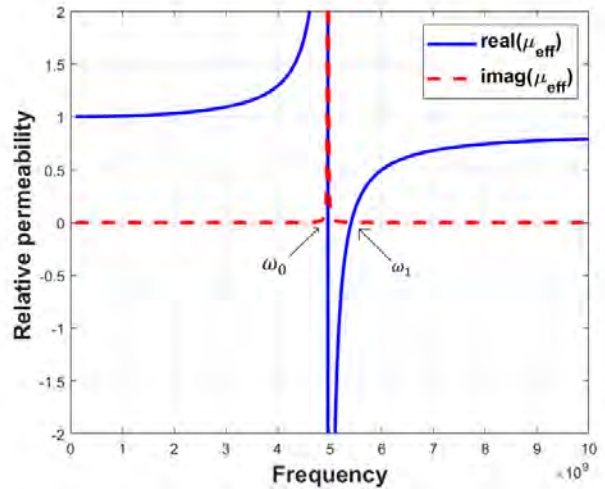
$$\omega_1 = \frac{2l\rho}{r\mu_0} \quad \dots \dots \dots (2b)$$



(a)



(b)



(c)

Figure 2.6: The frequency dependent permeability function for the split ring resonators presented in [24]. Fig. 2.6a is the terminology of each variable mentioned in equations (2a) and (2b). Fig. 2.6b is the frequency dependent μ for ideal ring loops, and Fig. 2.6c is when the loops have a finite resistivity.

Here ρ is the resistivity of the split ring material, and the geometrical meaning of other terms are described in Fig. 2.6a. Again, the imaginary part of the permeability is ideally zero, but acquires a huge positive value at the resonant frequency when the rings have finite resistivity.

The frequency vs. permeability curves are shown in Figs.2.6b and 2.6c, from where we see a small band of negative frequency zone, which resides within ω_0 and ω_1 .

Now, if we combine the periodic rod structure with the split rings and create a composite material [25], tune the key frequency points in equations (1) and (2), we can coincide the region of negative permittivity and permeability, we can simultaneously obtain negative values for both the electromagnetic properties, and the material could exhibit the peculiar effects described in [20]. These materials are modernly terms as double negative (DNG) material or left-handed materials (LHM), since the power flow does not follow the usual right-hand rule, rather follows the left hand rule.

A closer look at the Figs. 2.4 and 2.6 reveal that after the resonant frequency, both ϵ and μ are positive yet again. But at the neighborhood of the resonant point, this value is very low. So, in that neighborhood frequency, we expect the medium refractive index $\eta = \sqrt{\mu\epsilon}$ to be less than 1. What this implies is, in that case the metamaterial containing volume will have a refractive index less than the background medium (which is typically air), and which could allow the creation of an optically very light medium. This remarkable phenomenon was first highlighted in [26].

2.2.2 Resonant Cavities

The main idea of resonant cavities is to induce multiple reflection inside a finite volume (the cavity). The basic theory for ideal conducting plane and a point radiating source was first studied in [27]. There, a point source antenna was places between and infinite ground plane and a reflecting sheet with a reflection coefficient of $Re^{j\theta}$, where R is the magnitude of the reflection coefficient and θ is the phase alteration occurring at the boundary of the reflecting sheet. This infinite ground and the reflecting sheet form a cavity (See Fig. 2.7). Reflection from the sheet and the infinite ground ensures that any plane wave incident at an angle α will undergo an infinite number of reflections inside the cavity, enhancing electric field inside the cavity. At the same time, an enhanced amount of electric field will leak out, which is proportional to:

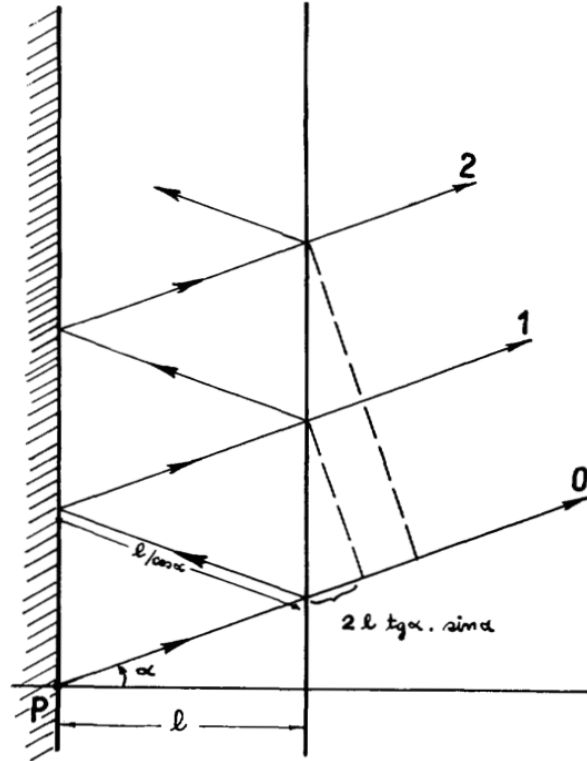


Figure 2.7: Geometric arrangement of an infinite resonant cavity [27]

$$E_{leak} \propto E_0 R^n \sqrt{1 - R^2} e^{j\Phi_n} \quad \dots \dots \dots (3)$$

Here, E_0 is the amplitude of the source wave. The phase angle of the n^{th} reflected wave can be written as:

$$\Phi_n = n \left[-\frac{4\pi}{\lambda} \cos\alpha - \pi + \theta \right] \quad \dots \dots \dots (4)$$

Inserting equation (4) inside equation (3) and further simplification results in:

$$|E_{leak}| \propto |E_0| \sqrt{\frac{1 - R^2}{1 + R^2 - 2R \cos(\theta - \pi - \frac{4\pi}{\lambda} \cos\alpha)}} \dots \dots \dots (5)$$

This leakage electric field is the field which is radiated because of the source wave. If the source is an antenna of arbitrary directive pattern $f(\alpha)$, we can replace the proportionality constant of equation (5) as:

$$|E_{leak}| = f(\alpha) |E_0| \sqrt{\frac{1 - R^2}{1 + R^2 - 2R \cos(\theta - \pi - \frac{4\pi}{\lambda} \cos\alpha)}} \dots \dots \dots (6)$$

Equation (6) describes that the amplitude of the leaked away wave is dependent on the reflecting nature of the reflecting sheet, the angle of incidence and the directive pattern of the source itself.

With the fundamental expressions of the metamaterials and the resonator cavities, we proceed to describe how they have shown the improve the directive gain of the antenna in the far field.

2.3 Antenna Gain Enhancement Mechanisms

2.3.1. The LHM Inverse Focusing Technique

In the frequency band where the periodic metamaterials exhibit negative ϵ and μ , there exist the peculiar phenomenon of waves refracting at a negative angle with the surface normal. This ends up the refracting waves focusing perfectly back on the direction of the source. In [28] this

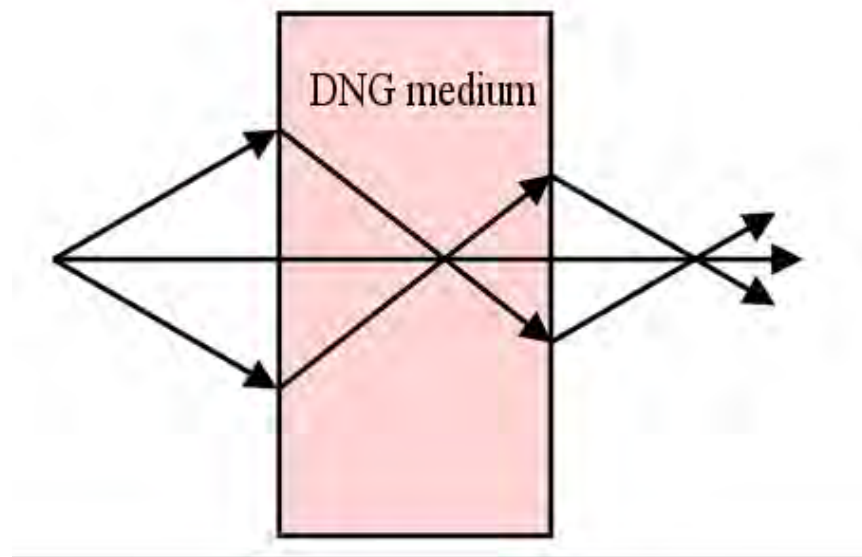


Figure 2.8: The inverse focusing effect inside a DNG material, where the focused waves end up directing along the central horizontal axis

phenomenon was described in considerable theoretical detail.

In a latter work [29], it was claimed that the perfect inverse focusing requires a refractive index of $\eta = -1$, which is very difficult to engineer for practical materials as it is impossible to obtain exact ϵ and μ values which would give the desired refractive index. In that work it has been shown theoretically, and demonstrated in simulation that in practice, when the refractive index is negative but not equal to -1 , there is still a partial inverse focusing phenomenon present, and the idea is applicable for paraxial angles.

For practical radiation sources, what this inverse focusing achieves, is a focal radiation along a particular direction (See Fig.2.8), which is precisely what a more directive transmission requires. Following the principle, a simulation demonstration was given in [30], and a full practical demonstration was found in [31], both have shown to provide considerable directive gain enhancement.

2.3.2 The Optical Lightning of the Source Medium

From the Figs.2.4 and 2.6, we see a region right after the resonant frequency of the DNG

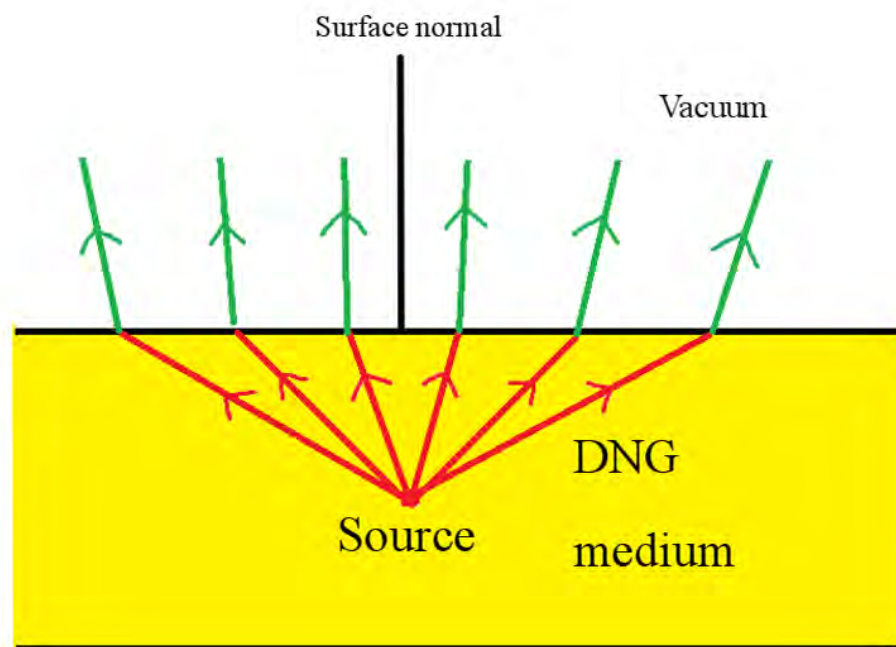


Figure 2.9: Wave incidence from a medium of lower refractive index than that of free space

material, where the ϵ and μ values are positive but less than one. It is this region, where the

refractive index becomes less than that of air [26]. Now, from ray optics theory it is well known that when radiation is incident on an optically denser medium, the waves come close to the surface normal. If we enclose the source in such an optically light medium, then all the waves incident along different angle will have a preferred direction along the surface normal, and this will end up making the source radiation directive (See Fig.2.9). The work of [26] applied this concept on a quarterwave monopole source antenna, which was surrounded by periodic rod structures to induce a medium with refractive index less than that of air. The directivity enhancement in that work was quite enormous. Later, [32] explored this concept on several other composite metamaterial geometries (See Fig. 2.10) at a frequency of **10 GHz** for short dipole source antennas and reported similar directive improvement. The design of the periodic structures involved the use of unit cells, with TEM (Transverse Electro Magnetic) wave incidence. For simulating the wave propagation, one pair of the unit cell boundaries is assigned as PEC (Perfect Electric Conductor), one pair as PMC (Perfect Magnetic Conductors) boundary, with a full wave port covering the surface, towards the directions of propagation (Fig. 2.10).

For the demonstration of directive gain enhancement on antennas, periodic structures were again chosen to be rod medium, but this time the periodic medium had a dielectric constant of 4. The authors reported two different “positions” of the source antenna with respect to the periodicity but showed that the gain enhancement is present for each of the two positions.

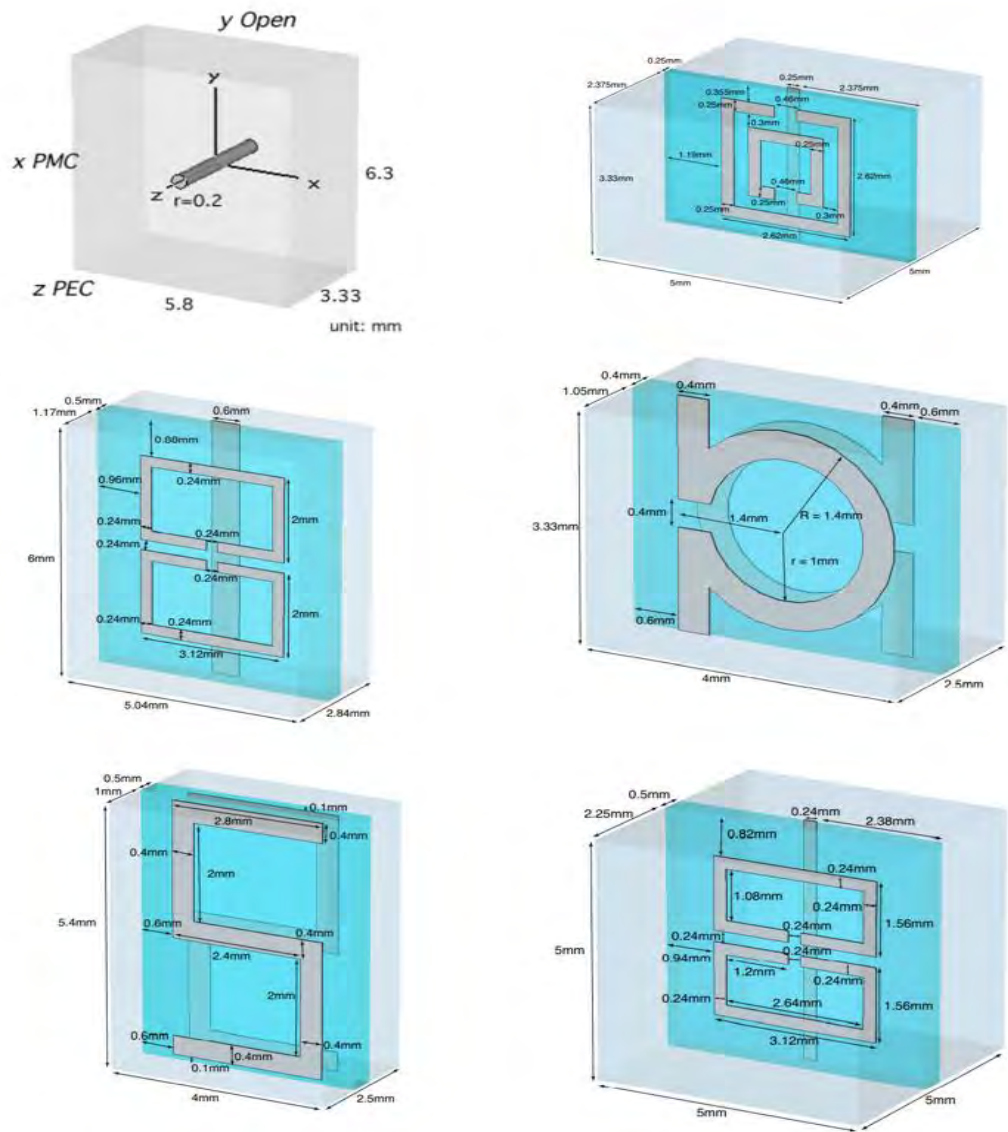


Figure 2.10: Different metamaterial unit cells to induce optical lightning effect [32]

2.3.3 The Fabry Perot Resonator Cavity Concept

Followed by the theoretical works in [27] and the examining equation (6), we can directly see that the formula points at the enhancement of directivity of any antenna within the cavity.

The antenna power pattern is directly proportional to the square of the electric field. So, the power pattern is directly proportional to E_{leak}^2 , and hence the pattern changes by a factor of

$$\frac{1 - R^2}{1 + R^2 - 2R \cos\left(\theta - \pi - 4\pi l \frac{\cos\alpha}{\lambda}\right)}$$

Now if we consider paraxial direction ($\cos\alpha \approx 1$), we can see that the maximum power is delivered when

$$\theta - \pi - \frac{4\pi l}{\lambda} = 0$$

Or,
$$l = \left(1 + \frac{\theta}{\pi}\right) \left(\frac{\lambda}{4}\right)$$

If the medium between the infinite ground and the infinite sheet is free space, then the reflection coefficient of the sheet will always induce a phase of $\theta = \pi$, which yields the optimum distance from the ground plane to the reflecting sheet as:

$$l = \frac{\lambda}{2} \quad \dots \dots \dots (7)$$

With the corresponding maximum gain of:

$$gain = \frac{1 + R}{1 - R} \quad \dots \dots \dots (8)$$

The equation (8) suggests, the more reflective the sheet is, the more the gain enhancement for the radiating antenna. The equation rises exponentially, and the gain enhances rapidly when the surface reflection is close to unity. (See Fig. 2.11).

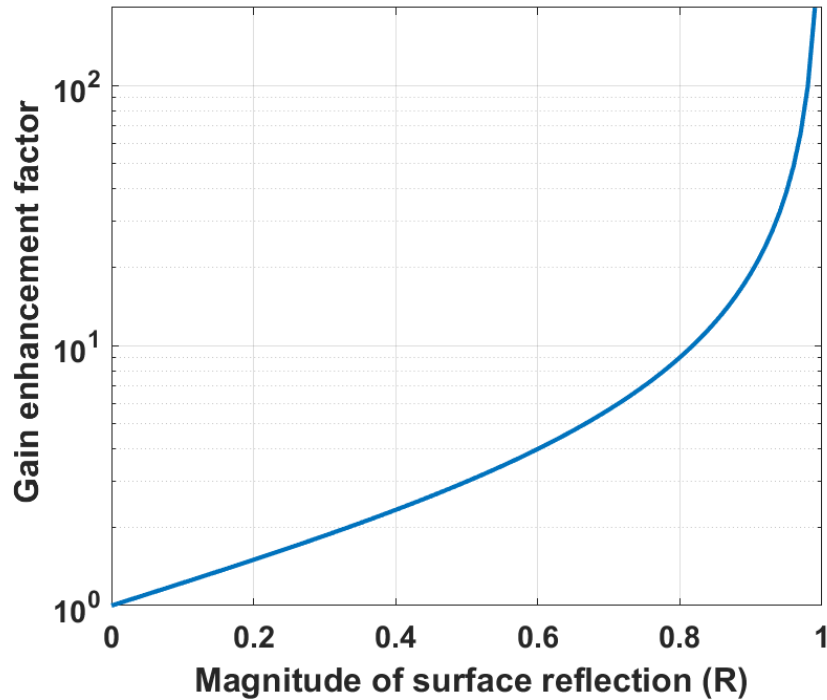


Figure 2.11: Gain enhancement of a source with a partially reflecting sheet above the ground

However, as the reflection reaches unity, the reflecting surface is no longer “partial”, and works as a PEC reflector. No waves leak out, the gain abruptly drops to zero and equation 8 becomes undefined.

The theoretical work was further enhanced in [33,34]. In [33], an attempt to make the partially reflecting sheet was carried out using “dipole-like rod arrays”, with the length of the rods optimized for a 15 GHz transmission enhancement. To form a paraxial incident with $\alpha = 0$, a rectangular waveguide aperture was used to form the radiating source (See Fig. 2.12). The configuration demonstrated through simulations and experiments that an optimized reflecting sheet can enhance both the directive gain and the bandwidth within a certain frequency range.

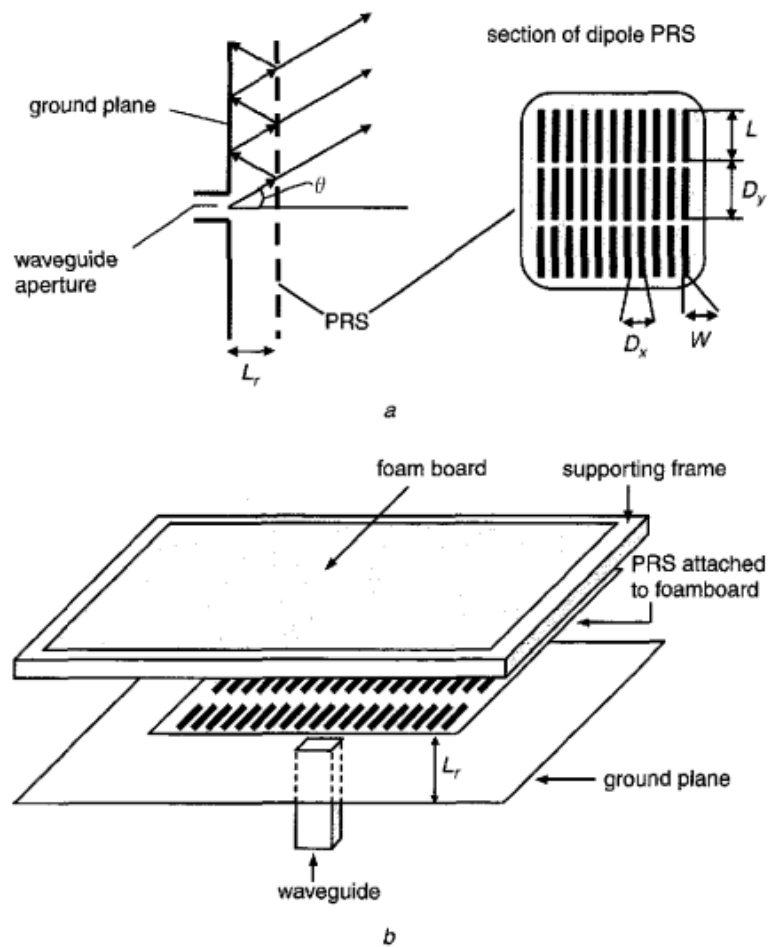


Figure 2.12: Practical realization of partially reflecting sheets to enhance transmission gain [33]

In [34], the distance between the source and the ground has been reduced from $\frac{\lambda}{2}$ to $\approx \frac{\lambda}{4}$ using metamaterial ground planes (MGP) instead of using a PEC ground plane, which exploited the negative refractive properties of the metamaterials which has been discussed in section 2.2.1. Unit cells of simple square patch arrays has been used, which obtained a significantly reduced profile.

However, for practical consideration, producing a reflecting “sheet” with controlled reflection coefficient is not very feasible. Even in the experiments in [33], foam superstates (which has very low permittivity) were used to support and suspend the sheet array at the desired location. Such complicated arrangement is not desirable in biosensing, as suspension objects will induce unnecessary complications. So, instead of using the reflecting sheets, it is more convenient to use dielectric superstrates above the source at the optimum distance.

The magnitude of the reflection coefficient at a surface is related with the impedance mismatch between the two media at the two sides of the surface. The more impedance mismatch, the higher the reflection. When we apply superstrates, it creates an impedance mismatch with the external media (air) and the mismatch is more when the permittivity is higher. Therefore, the higher the permittivity of the superstrate, the more reflective it will become, and there will be more gain enhancement. A study considering infinite ground, with single and multiple superstrate configuration agrees with the idea [35], and it has been shown that the directivity enhancement is almost linear with the increase of superstrate permittivity. The study also show that multiple superstrates can provide better directivity enhancement, which is expected since multiple reflecting sheets will increase the overall reflection and create another resonant cavity (See Fig. 2.13). However, regarding that idea to enhance gain between closely separated antenna pairs, there are two issues:

- Ideal patches with infinite ground plane had been assumed, a physical approximation of which requires a large antenna plane, which is not a feasible idea for small domain applications such as biosensing. Therefore, we need to explore what a finite ground with superstrates has to offer in terms of transmission performance.

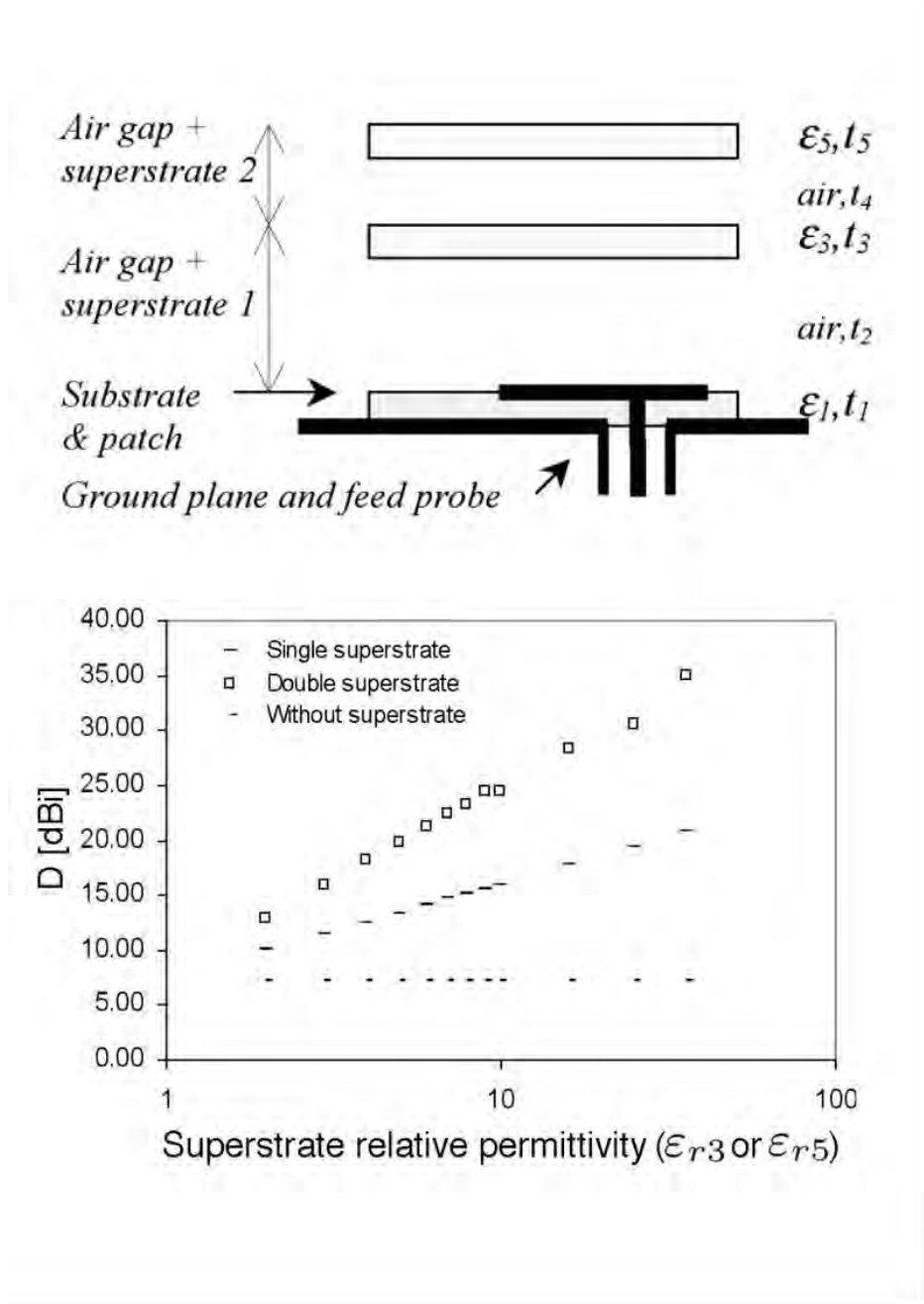


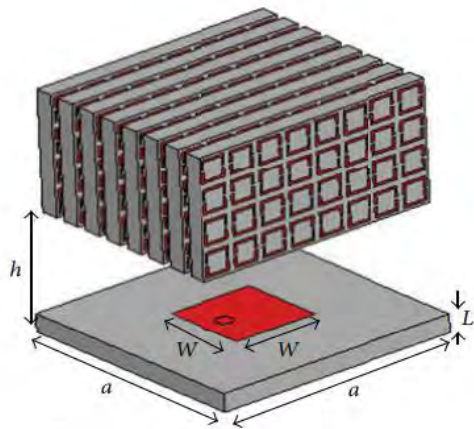
Figure 2.13: Simulations with single and multiple superstrates above an infinite ground plane, and the enhancement of directive gain [35]

- The addition of the superstrate with single or multiple layers, add another unknown variable, which is the superstrate dielectric constant. In the work of [35], the thickness of the superstrate was assumed to be $\frac{\lambda}{4\sqrt{\epsilon_{sup}}}$, where ϵ_{sup} is the superstrate dielectric constant. This formula gave an approximate optimum thickness which works for a superstrate dielectric constant of 3, but for finite size antenna and variable superstrate dielectric constant, this value needs to be optimized.

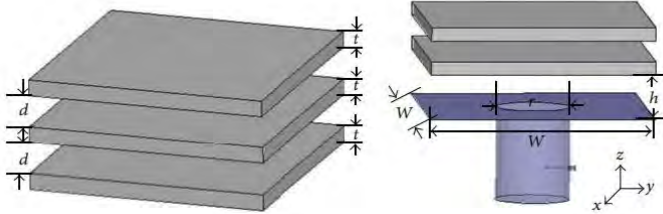
Fig. suggests that in order to induce very high gain, the superstrate dielectric constant need to be very high, whereas such dielectric materials may not be available commercially. In a subsequent work [36], it has been shown that the inclusion of the conducting imprints on the superstrate surface can enhance the reflectivity and the superstrate would offer higher reflection than the material itself. Since the reflective nature of the material is modified in the process, it is also termed as “metamaterial”. The metamaterial unit cells were simple square patches which were very easy to fabricate and implement. However, the dimension of the ground planes in these works were still very large.

In a further work [37], the effect of metallic imprints on superstrates was investigated in further detail, and the resonator cavity concept was applied on a finite sized patch antenna with finite ground. There it has been shown that the increase of gain is not indefinitely proportional to the surface reflection as equation (8) would suggest, rather the gain enhancement has a certain limit.

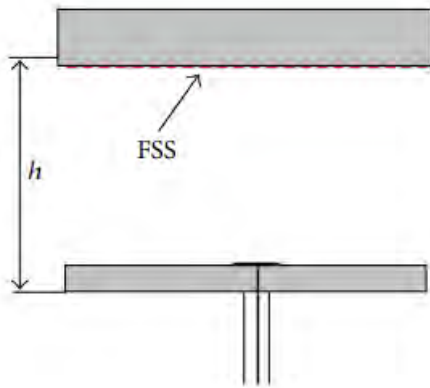
Three types of metamaterial effects were observed; the LHM inverse focusing technique, the effect of multiple superstrates, and the inclusion of square patch FSS (Frequency Selective Surfaces) below the superstrates (See Fig. 2.14).



(a)



(b)



(c)

Figure 2.14: Three different gain enhancement techniques on finite sized patch antenna. Fig. 2.14a is the use of stacked periodic structures to form LHM, Fig. 2.14b is the use of multiple superstrates, and Fig. 2.14c is the use of FSS imprints at the bottom of the superstrates.

The LHM focusing method does not depend on any superstrate reflection, however, the other two does depend, and the simulation results show that for smaller sized patches the relation mentioned in equation (8), (or demonstrated in Fig. 2.11) does not hold. Rather, after a certain amount of superstrate reflection, the gain drops abruptly (See Fig. 2.15)

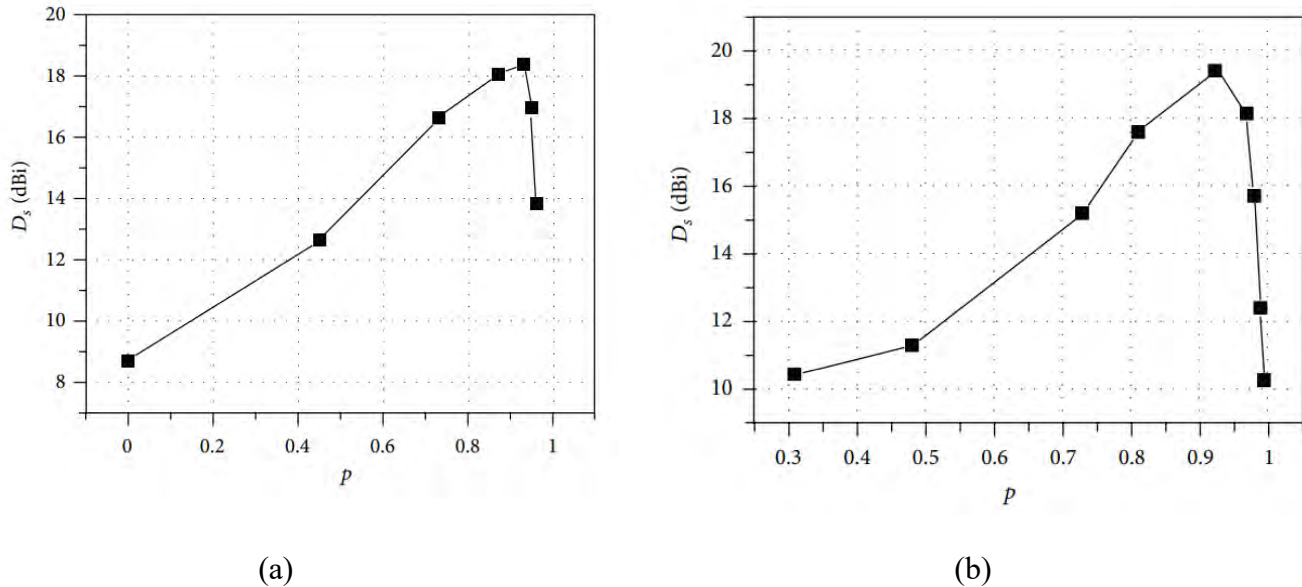


Figure 2.15: Effect of superstrate reflection on the directive gain enhancement of finite sized antenna [37].

Fig. 2.15a is for the multiple superstrate configuration, Fig. 2.15b is for the FSS configuration

Following the findings, the concept of “optimum reflection coefficient” was proposed in the work, which claims that until a certain amount of increase in superstrate reflection, the gain will increase, but then the gain will decrease very rapidly. So, the task of the metallic imprinter designer is to make the superstrate acquire the optimum reflection coefficient through the inclusion of the imprints.

2.4 Possible Expectations in the Biosensing Application

While we laid down some of the concepts of directivity enhancement in for radiation, we also need to describe which of the following options is a feasible technique for the biosensing systems.

The concept of LHM inverse focusing requires the design to operate within a very small frequency band. In addition, the periodicity must be along the direction of propagation, which will require huge spatial requirement. The same problem persists if we try to implement the idea of optical lightening of the source media. To make things worse, in the near field, the two antennas are very closely coupled with complicated polarizations, which makes the operating frequency vary with small misalignments of the antenna pairs. So, these two ideas fare poor in terms of practicality.

What is left is the Fabry Perot concept, which might have some positive effect on the transmission enhancement of the antenna pairs. The primary merit of the idea is that the governing principle is not directly related to the operating frequency, and only depends on the reflecting nature of the superstrate. But on the other hand, there is also a major hurdle to overcome. Since the optimum distance between the antenna and the superstrate is $\frac{\lambda}{2}$, we are forced to increase the distance between the antenna pairs. However, increasing the antenna separation result in the reduction in antenna coupling and less transmission. So, the possible gain in performance must surpass, or at least be comparable to the loss of transmission due to the increase of antenna pairs, and ultimately achieve an overall increase in transmission between the antennas.

Since in this work we investigate the same concept on the transmission characteristics between two antennas, the above discussions boil down to the following expectations:

- With the increase of superstrate permittivity, transmission will enhance but only up to a given maximum superstrate permittivity.

- Insertion of metamaterial imprints on low permittivity superstrates can produce the optimum performance at a higher permittivity. This tool can be especially useful since practical high permittivity materials are not always commercially available, and they provide relatively large dispersive loss.

Chapter 3

Analysis of the Transmission Characteristics

In this section we present appropriate simulation studies, based on the gain enhancement methods described in the previous section. Based on the study, our exploration boils down to the following expectations:

- With the increase of the superstrate dielectric constant, transmission will enhance but only up to a given maximum superstrate permittivity.
- Insertion of the metamaterial imprints on the low permittivity superstrate can replicate the performance of the optimum permittivity and yield similar transmission performance. The thickness of the superstrate for the given dielectric constant can be optimized through parametric analysis.

Along with exploring these results, we also propose and investigate the effect of filling the patch-superstrate gap with dielectric materials. The idea came up with two motivations:

- The insertion of the dielectric material turns the patch-superstrate gap into a dielectric waveguide channel, where some of the leaky waves can reflect into the channel and increase the number of reflections, and possibly the overall transmission. (See Fig.3.1)
- The effective half wavelength distance from the source to the superstrate will be now reduced to $\frac{\lambda}{2\sqrt{\epsilon_{gap}}}$, where ϵ_{gap} is the dielectric constant of the gap filled material. As a result, the system bulk will be miniaturized, which is always desirable in the implementation of biosensing systems.

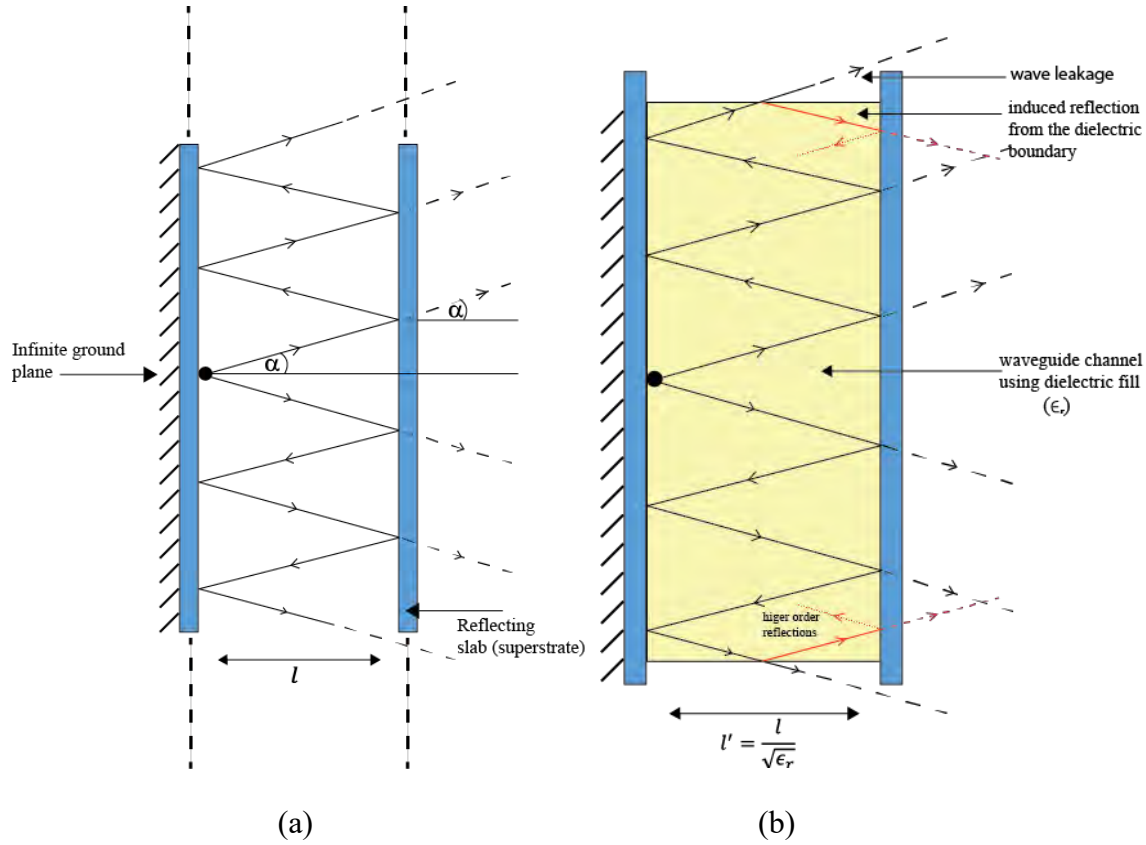


Figure 3.1: Geometric interpretation of the Fabry Perot resonator concept with the proposed idea. In Fig. 3.1a, the waves leak away from the top and bottom sides, which is reflected back inside to induce further reflection in Fig. 3.1b

3.1 Simulation Systems for Examining Transmission Enhancement

In our research, we shall analyze the performance enhancement in transmission due to the variation in the following variables:

1. The dielectric constant of the superstrate (ϵ_{sup})
2. The effect of the gap insertion material which has a dielectric constant of ϵ_{gap}
3. The effect of metamaterial ring imprints on the superstrate.

Throughout the analysis, the operating frequency will be fixed at 4.8 GHz, and both the implant and the external antennas will be tuned to that frequency.

Throughout the analysis, we have noticed that the resonant frequency of the two antennas change with the variation of each of the three variables mentioned above. Therefore, we refrain to explicitly define the dimensions of the antenna geometries, and only focus on their relative distance and the construction of the system.

We will explore two different antenna pair configurations and examine transmission characteristics on each of them to draw the necessary conclusion. For the analysis, we assume that the two antennas are simple patch antennas with line feeding technique. Patch antennas are relatively straightforward to design with the equations of the dimensions available in [19], and since throughout the analysis we needed to tune the antennas continuously, we chose to resort to the simplified designs (See Fig. 3.2). We choose to design the dimensions (L_1 and W_1) of the patch antenna using the following equations:

$$W_1 = \frac{c_0}{2f \sqrt{\left(\frac{\epsilon_r + 1}{2}\right)}} \quad \dots \dots \dots (9a)$$

$$\epsilon_{eff} = \frac{\epsilon_r + 1}{2} + \frac{\epsilon_r - 1}{2} \left(1 + \frac{12h}{W}\right)^{-\frac{1}{2}} \quad \dots \dots \dots (9b)$$

$$L_{eff} = \frac{c_0}{2f \sqrt{\epsilon_{eff}}} \quad \dots \dots \dots (9c)$$

$$\delta_L = \frac{0.412h (\epsilon_{eff} + 0.3) \left(\frac{W}{h} + 0.264\right)}{(\epsilon_{eff} - 0.258) \left(\frac{W}{h} + 0.8\right)} \quad \dots \dots \dots (9d)$$

$$L_1 = L_{eff} - 2\delta_L \quad \dots \dots \dots (9e)$$

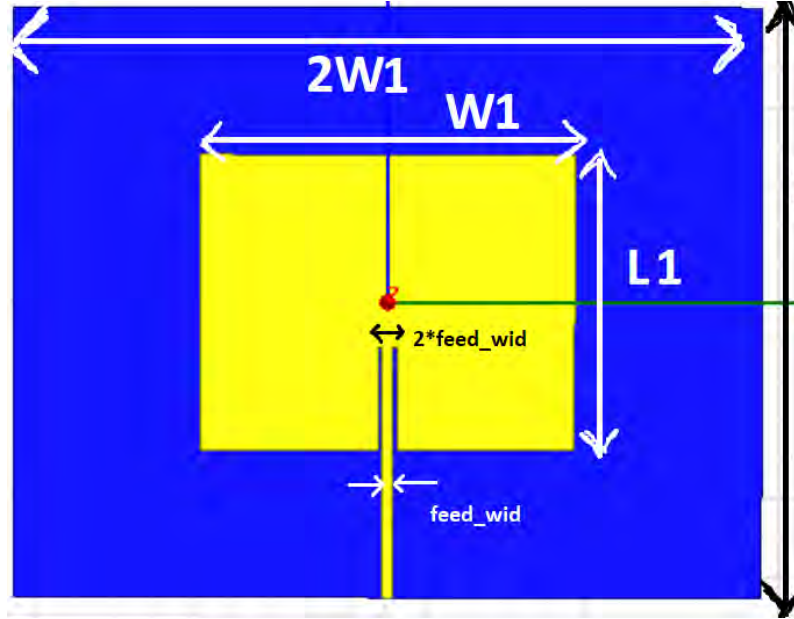


Figure 3.2: Simplified antenna geometry for the analysis of the transmission performance in the simulation systems.

Here, f is the frequency of operation, and h is the thickness of the substrate, which is $0.762m$.

ϵ_r is the dielectric constant of the substrate material, which is chosen to be 3.5 in the design.

Using equations in (9) we choose the initial dimensions of the antennas, and from there on, optimize the design to resonate at the desired $4.8 GHz$ frequency. In all the designs, the ground covers the total surface of the other side of the substrate.

The first antenna pair system is the simple one, where the two antennas are separated in free space, whereas, in the second antenna pair system one antenna is buried inside a dispersive material, which resembles a biological tissue. The material has an assumed dielectric constant of $\epsilon_{tissue} = 40$ and a conductivity of $\sigma_{tissue} = 3Sm^{-1}$ at $4.8 GHz$, which is similar to most biological tissues [38]. For clarity's sake, we denote the two systems as “system 1” and “system 2” respectively (See Fig. 3.3).

For each of the two systems, we analyze the transmission characteristics in the following steps:

- First, we take note of the transmission loss for the two systems, keeping the antenna pairs only. This will serve as the preliminary benchmark of the transmission performance, and we will compare the performance improvement in the following steps with respect to the baseline.

For system 1, the two antennas are separated by a wavelength distance $\lambda_{air} \approx 62.5 \text{ mm}$ in free space. For system 2, the biological tissue medium boundary is placed

at a distance $3 \frac{\lambda_{air}}{4} \approx 46.875 \text{ mm}$ in front of the external antenna. The second

antenna is buried further a distance $\frac{\lambda_{tissue}}{2} = \frac{\lambda_{air}}{2\sqrt{\epsilon_{tissue}}} \approx 4.94 \text{ mm}$ inside the

tissue medium (See Fig. 3.3a)

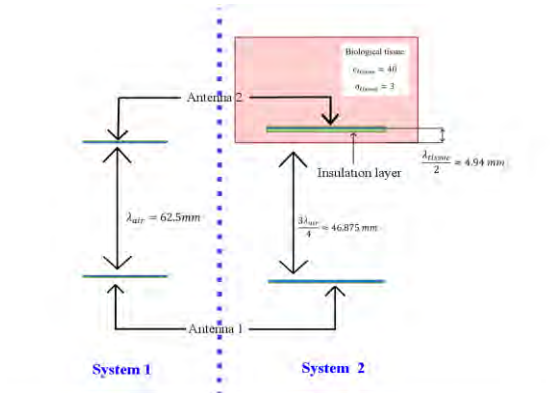
- In the next step, we add a superstrate layer between antenna 1 and antenna 2. According to the Fabry Perot resonator cavity theory described in section 2.3.3, the patch to superstrate distance is half wavelength, which is $\frac{\lambda_{air}}{2} \approx 31.25 \text{ mm}$. So the

superstrate layer was placed 31.25 mm in front of antenna 1 in both systems. Distance between the two antennas is remained unchanged, also for the two systems (See Fig. 3.3b). After the arrangement, we vary the superstrate dielectric constant ϵ_{sup} and take note of the transmission curves.

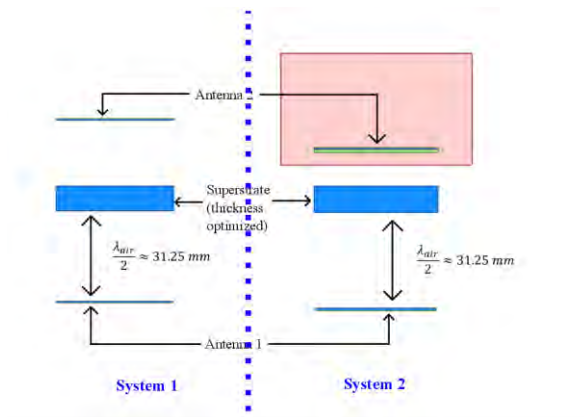
- Next, we fill the gap between antenna 1 and the superstrate with a dielectric material which has $\epsilon_{gap} = 2$. To maintain the same half wavelength cavity, the new air-

superstrate gap is now $\frac{\lambda_{gap}}{2} = \frac{\lambda_{air}}{2\sqrt{\epsilon_{gap}}} \approx 22.09 \text{ mm}$ (See Fig. 3.3c). In this way,

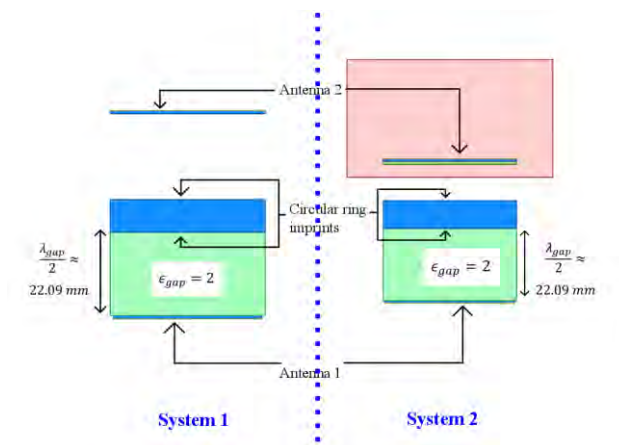
although the distance between the antenna and the superstrate is reduced, the overall wavelength distance is kept the same. We again vary ϵ_{sup} and observe the transmission performance.



(a)



(b)



(c)

Figure 3.3: Step by step schematic diagram for the analysis of the two define antenna system. In Fig. 3.3a, the two antennas are separated without any engineering in between. In Fig. 3.3b the superstrate material is inserted between the two antennas. In Fig. 3.3c the air superstrate gap is filled with a material with dielectric constant of 2.

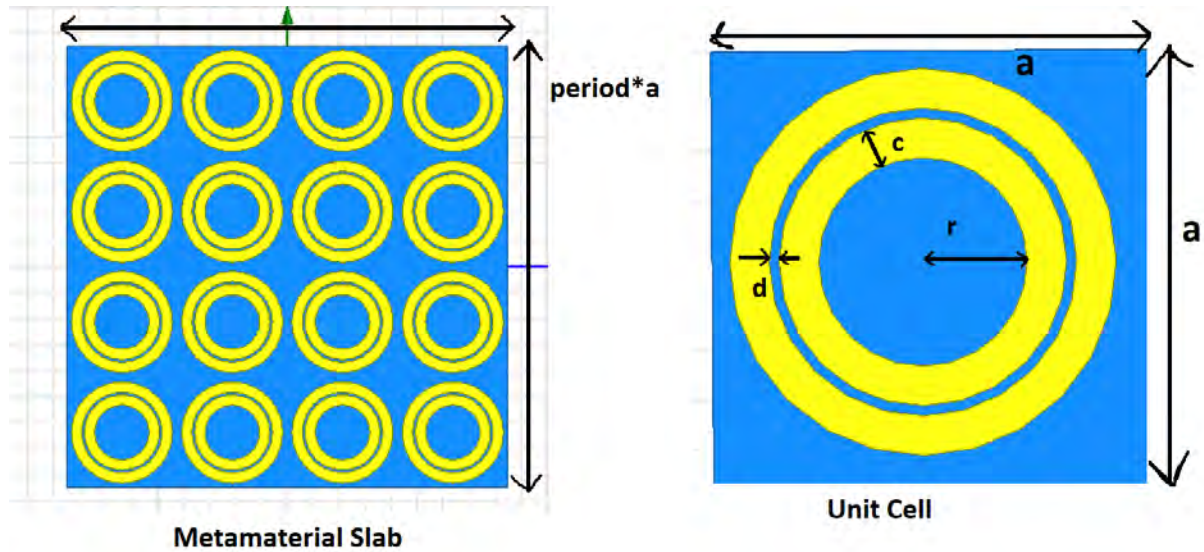


Figure 3.4: The top view of the metamaterial imprinted superstrate and the unit cell. The reflectivity can be tuned by varying r, c, d

- Finally, we add circular ring metamaterial imprints on both sides of the superstrate for a relatively low ϵ_{sup} to enhance superstrate reflection and generate at least similar transmission characteristics. The geometry of the metamaterial imprints on the two surfaces is shown in Fig. 3.4.

For the metamaterial imprints, we choose simple circular rings. The amount of reflection from the surface can be made large or small depending on the metallic surface, which is the area covered by the metallic imprints. A larger area of metallic imprint in the unit cell will add more reflection over the surface.

We also present the antenna dimensions (See Table 3.1) which we have used in each of the steps, for both the systems. Since the inclusion of dielectric insertions, coating materials and superstrates altered the location of the resonant points, the dimensions had to be updated in order to keep the resonant point fixed and to get a proper comparison.

TABLE 3.1: DIMENSIONS OF THE TWO ANTENNAS FOR EACH SYSTEM, AND FOR EACH STEP OF THE ANALYSIS. ALL UNITS ARE IN MM

	System1	System2
Step 1	L1 = 15.97, W1 = 20.21 L2 = 15.97, W2 = 20.21	L1 = 16.03, W1 = 20.29 L2 = 15.87, W2 = 20.29
Step 2	L1 = 15.97, W1 = 20.21 L2 = 16.03, W2 = 20.29	L1 = 16.03, W1 = 20.29, L2 = 15.87, W2 = 20.29
Step 3	L1 = 15.4, W1 = 19.5 L2 = 16.03, W2 = 20.29	L1 = 15.71, W1 = 19.88, L2 = 15.87, W2 = 20.29
Step 4	L1 = 15.45, W1 = 19.5 L2 = 16.03, W2 = 20.29	L1 = 15.71, W1 = 19.88, L2 = 15.87, W2 = 20.29

In addition to all of that, in system 2, we have also covered the patch of the implant antenna (antenna 2) with a 1.5mm thick layer of polydimethylsiloxane (PDMS) insulation, which is a real dielectric material ($\epsilon_r = 2.8, \tan\delta = 0.002$). It has been shown that such coating not only ensures biocompatibility but also improves the transmission significantly by reducing dispersion loss inside the lossy medium. [16,39]. To illustrate this, the amount of transmission

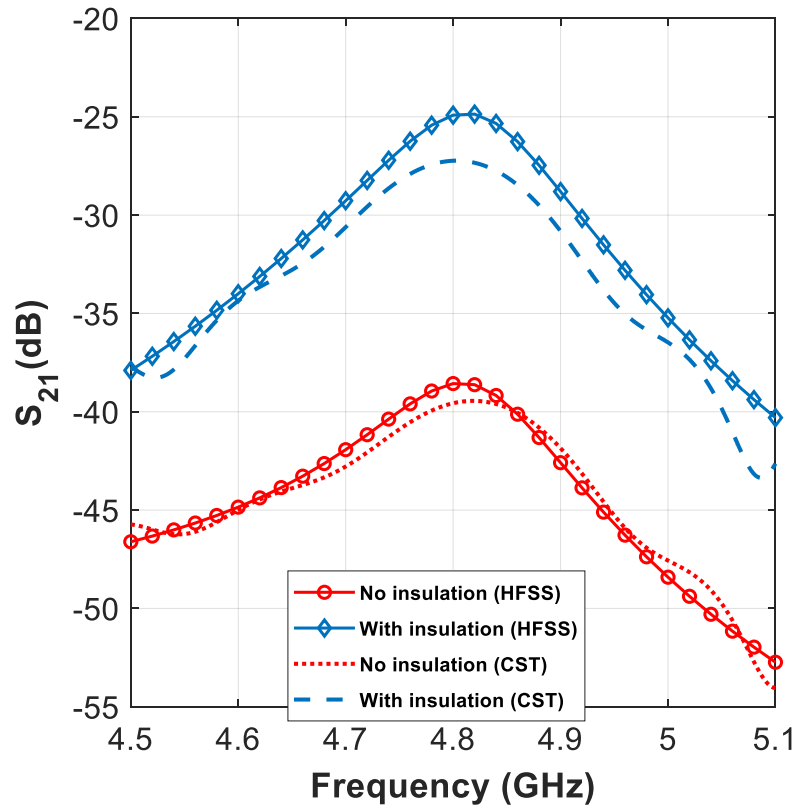


Figure 3.5: Effect of insulation coating to enhance transmission gain.

loss with and without the present of the insulation coating is presented in Figure 3.5, from which a transmission enhancement of ≈ 14 dB can be observed.

3.2 Transmission Analysis

In this section, we present the simulation results for each of the two systems in each step, which has been mentioned in the previous section:

For system 1, the initial transmission was found to be -9.33 dB . After adding superstrate, the transmission improved. At first, the performance improved with the increase of the superstrate

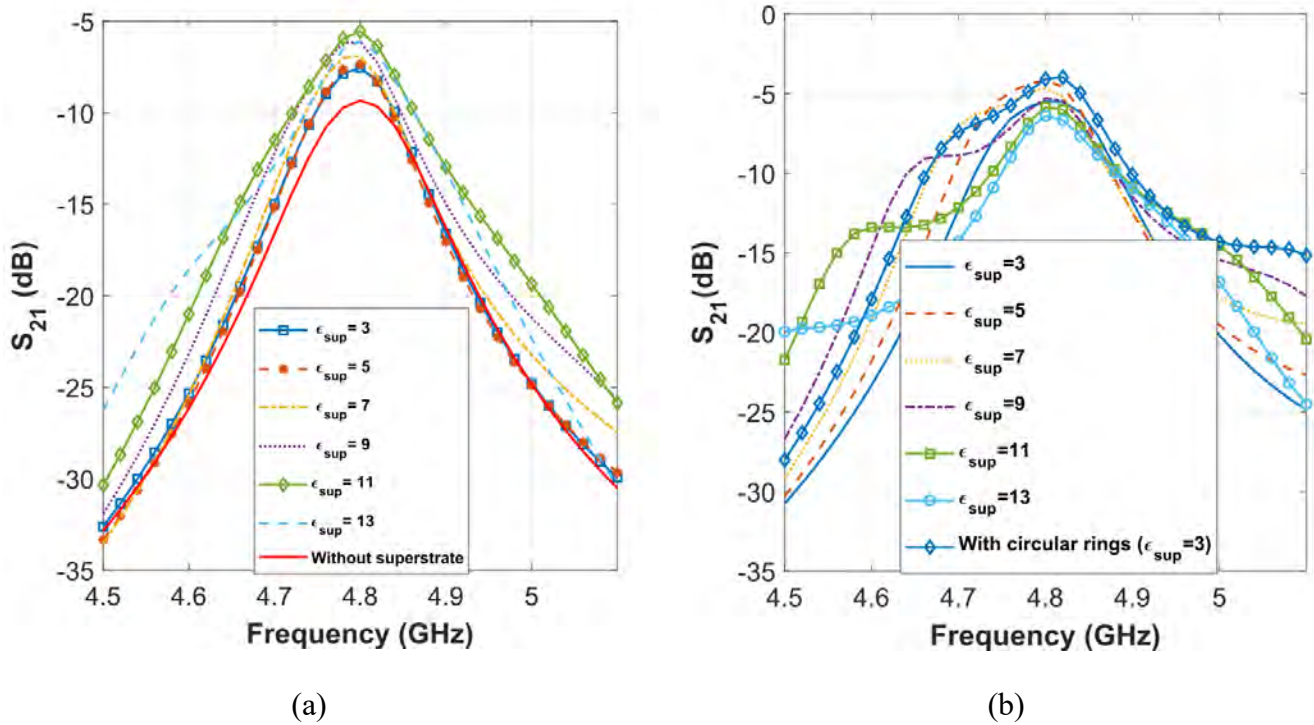


Figure 3.6: Effect of transmission enhancement with varying superstrate dielectric constant for system 1, Fig. 3.6a is the effect of superstrate inclusion, and Fig. 3.6b is the effect after the inclusion of gap material and circular rings.

dielectric constant, and the best transmission was found to be -5.54 dB for $\epsilon_{sup} = 11$, which is an improvement of around $\approx 3.8 \text{ dB}$. However, after the superstrate dielectric constant increase further, we see a fast reduction in the transmission performance (See Fig. 3.6a).

Therefore, we indeed find the maximum limit of superstrate permittivity (reflection) for which the transmission is maximum.

Next, after filling up the patch-superstrate gap with dielectric, we again see a secondary improvement in transmission performance. The best transmission is found to be $\approx -4.08dB$, for $\epsilon_{sup} = 5$. Later, after adding circular rings on both sides of the superstrate, we obtain similar

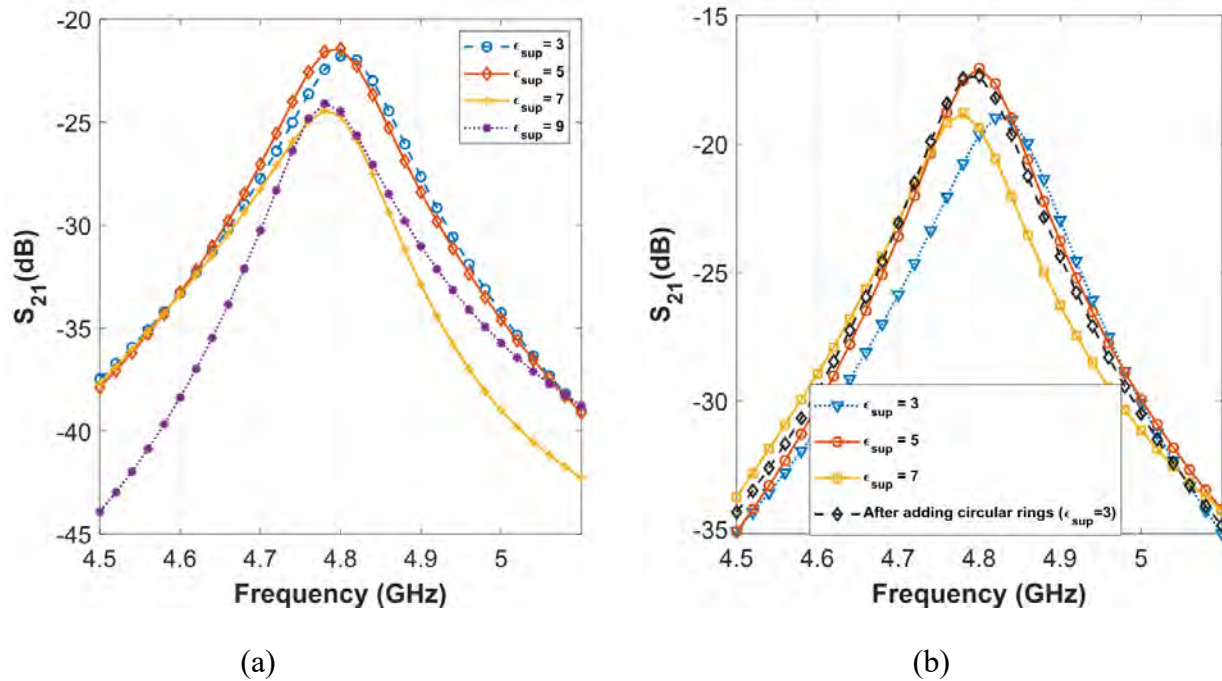


Figure 3.7: Effect of transmission enhancement with varying superstrate dielectric constant for system 2, Fig. 3.7a is the effect of superstrate inclusion, and Fig. 3.7b is the effect after the inclusion of gap material and circular rings.

performance but for $\epsilon_{sup} = 3$ (See Fig. 3.6b). From the final transmission curve, we find that a total improvement of over 5 dB has been achieved after all these steps.

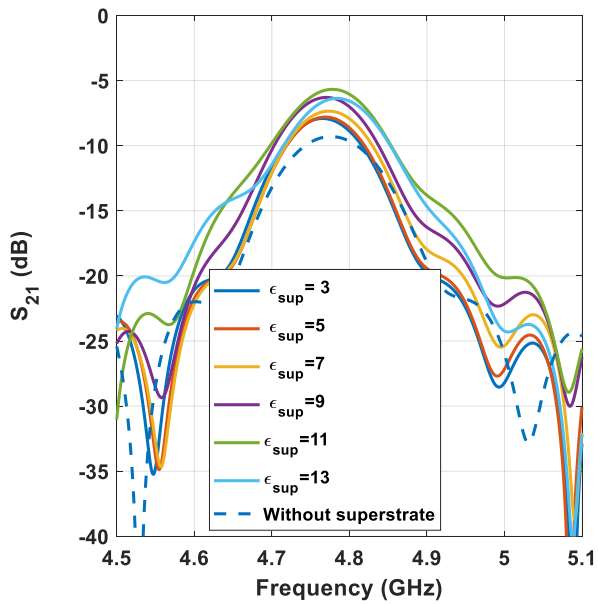
For system 2, the initial transmission loss after the inclusion of insulation layer was found to be -24.1 dB (See Fig. 3.5). From there on, the performance improved with the inclusion of superstrates, and reached a maximum of -21.7 dB for $\epsilon_{sup} = 5$. (See Fig. 3.7a). Further increase of ϵ_{sup} degraded the transmission performance. Later, after filling the patch superstrate gap with dielectric material, the transmission improved yet again. The maximum transmission gain was noted to be -17.06 dB for $\epsilon_{sup} = 5$. Finally, after adding circular rings on the superstrates, we obtain similar performance for $\epsilon_{sup} = 3$ (See Fig. 3.7b). Therefore, a total transmission enhancement of around 8 dB has been achieved for system 2.

3.3 Verification

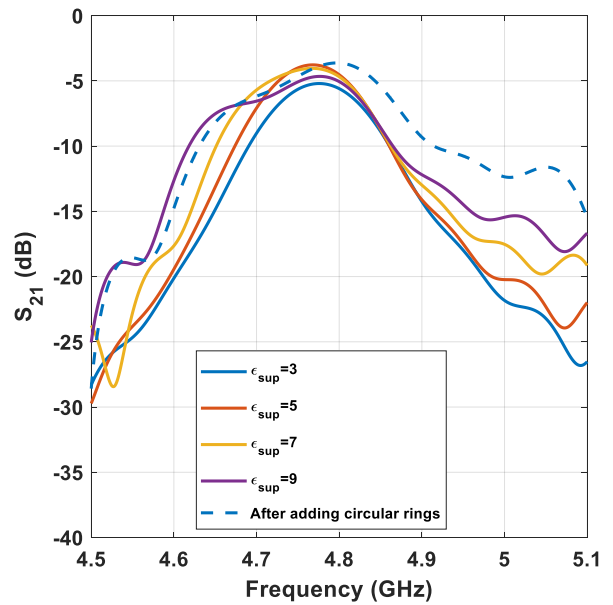
In this section, we proceed to validate the results with similar simulations in CST Microwave studio. HFSS performs simulations using 3D full wave finite element method, while CST studio uses multiple methods to simulate a given environment. Two of the most common used simulation techniques are time domain and frequency domain analysis. Among the two of them, we have used time domain simulations to verify the results due to its relative speed compared to the frequency domain simulations. The time domain solver also uses a different simulation technique, which is called the “Finite Integration Technique (FIT)” which is different from the Finite Element Method (FEM) analysis in HFSS. Therefore, a good validation match would ensure that the proposed methodology is indeed applicable.

For system 1, the initial transmission is found to be -9.30 dB , which enhanced to -5.67 dB at a maximum superstrate permittivity of 11. After the inclusion of dielectric insertion, the performance further improved to -3.78 dB for a superstrate dielectric constant of 5. Finally, after adding the circular ring on both sides of the superstrate, a similar performance of -3.63 dB has been obtained (See Fig. 3.8).

For system 2, the initial transmission after adding the insulation layer is found to be -27.2 dB , which enhanced to -23.9 dB at a maximum superstrate permittivity of 5. After the inclusion of dielectric insertion, the performance further improved to -19.36 dB for a superstrate dielectric constant of 5. Finally, after adding the circular ring on both sides of the superstrate, a slightly better performance of -18.53 dB has been obtained (See Fig. 3.9).

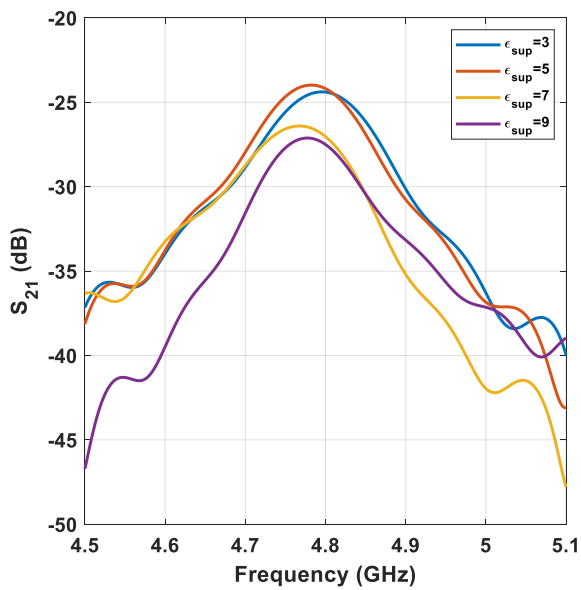


(a)

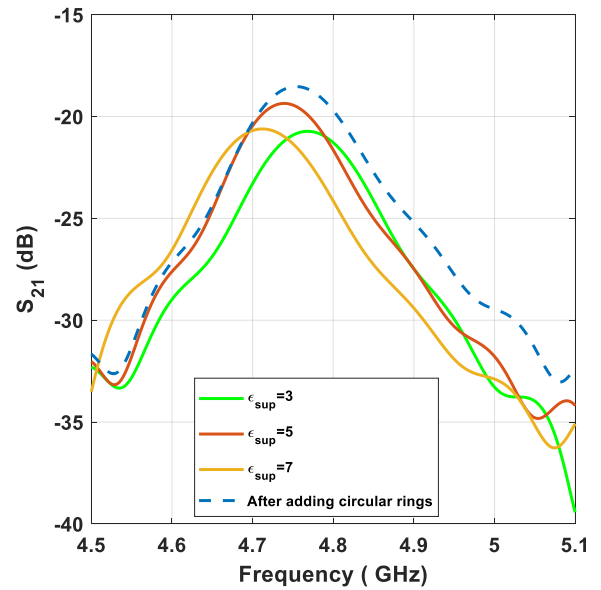


(b)

Figure 3.8: Verification of Figs. 3.6a and 3.6b with CST Microwave Studio



(a)



(b)

Figure 3.9: Verification of Figs. 3.7a and 3.7b with CST Microwave Studio

From the verification we can see that the transmission performance, and the enhancement after each step, agree very well between the two software, thereby assuring the correctness of the experiments. The slight discrepancies are mainly because of the two different simulation mechanisms, and the different excitation ports which has been used in the two simulators.

3.4 Summary

After exploring the effect of the superstrate, the gap filler material, and the effect of metamaterial imprints on both sides of the superstrate, we can draw the following conclusions:

- The overall transmission increases with the inclusion of the superstrate material. The increase is not indefinite, rather reached a maximum for a given superstrate dielectric constant. This maximum limit depends on the antenna pair configuration and the background medium. Afterwards the transmission degraded very quickly.
- Filling up the patch superstrate gap with dielectric filling further enhances transmission. Once again, there is a maximum limit of superstrate dielectric constant to be found, at which the transmission is maximum and later the performance degrades.
- The inclusion of metamaterial imprints on the superstrate enables to replicated high dielectric constant superstrate effect on relatively low value superstrates.

The optimum reflection can occur at a very high value of superstrate dielectric constant. For example, in system 1, we see that the maximum transmission occurs at a superstrate dielectric constant of 11. Practically, high permittivity materials are usually dispersive in nature, and hard to produce. The inclusion of metamaterial imprints allows the problem to be overcome and induce similar performance on commercially available low value and low dispersive dielectrics.

Chapter 4

Potential of the Proposed Concept in Biosensing

Having explored the potential of the superstrate, the dielectric insertion, and the metamaterial imprints on the transmission curve, we proceed to design and propose a proof-of-concept design, which can resemble communication for biological sensing. For this purpose, we need to design the simulation environment with such materials, that are practically available, and also properly model each of the transmission medium.

For the proof-of-concept design, we use both HFSS and CST studio to simulate and verify the proposed design. The complete design is done in the following steps:

- Design of the simulation environment
- Design of the antennas
- Design of the superstrate, and metamaterials.

After the design and simulation is complete, we also proceed to evaluate the performance comparing it with some of the existing literature.

4.1 Designing the Simulation Environment

For the design, we have performed full wave simulations. The background was modelled with a radiation box (in HFSS), which has the dimension of $2\lambda_{air} \times 2\lambda_{air} \times 2\lambda_{air}$, here within which the full simulation geometry could be incorporated with additional distance of above $\frac{\lambda_{air}}{4}$ in each direction so that the radiation boundary can work properly. The biological tissue is

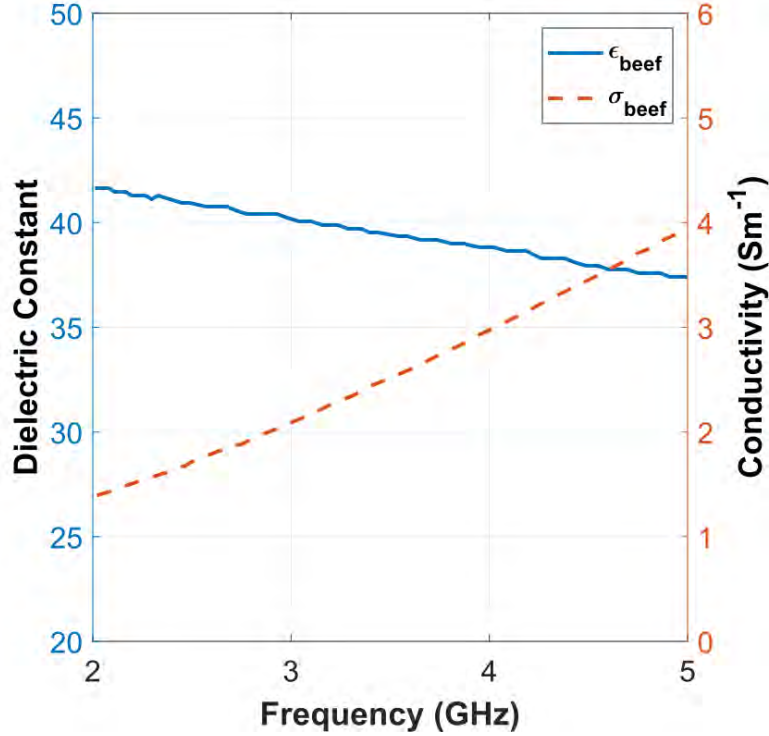
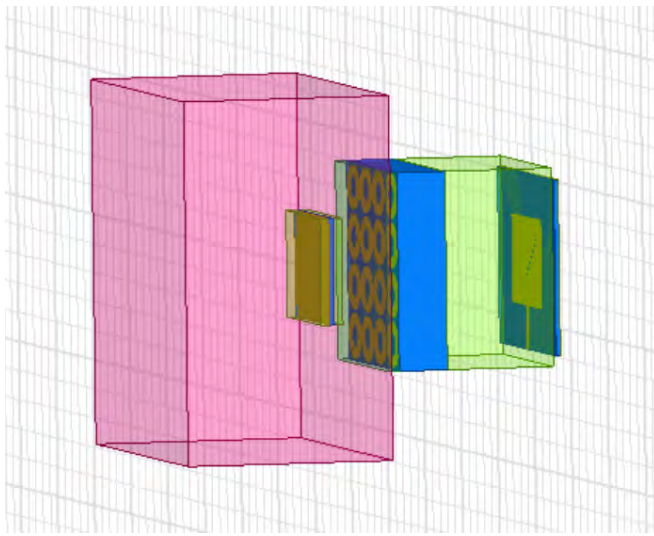


Figure 4.1: Frequency dependent dispersive biological tissue with dielectric properties similar to ground beef [16]

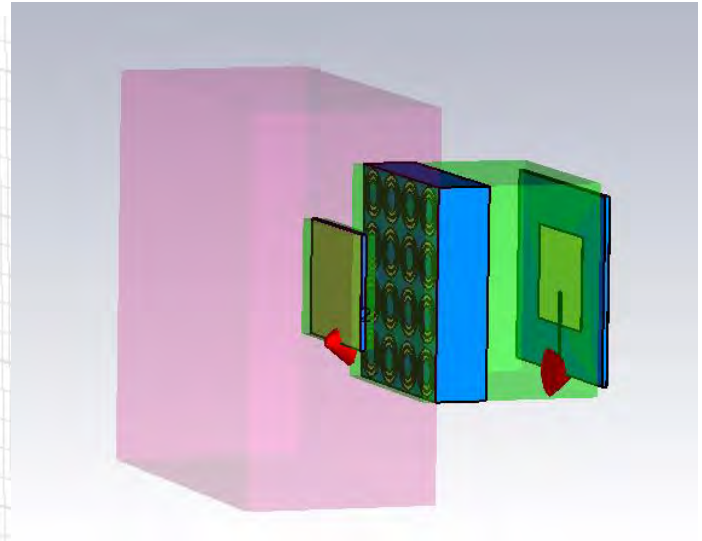
modelled to be frequency dependent similar to [16], and we directly extracted the values from the particular reference (See Fig.4.1). In the model, the dielectric constant slowly degraded with increasing frequency, and the conductivity was linearly increasing with frequency. Our focus of interest was again, the behaviour at 4.8 GHz.

The biological tissue was assumed to have a dimension of $\lambda_{air} \times \lambda_{air} \times \frac{\lambda_{air}}{2}$. The apparently large dimension of the biological tissue ensured that the size is much larger than the antenna dimensions and we need not worry about boundary radiation.

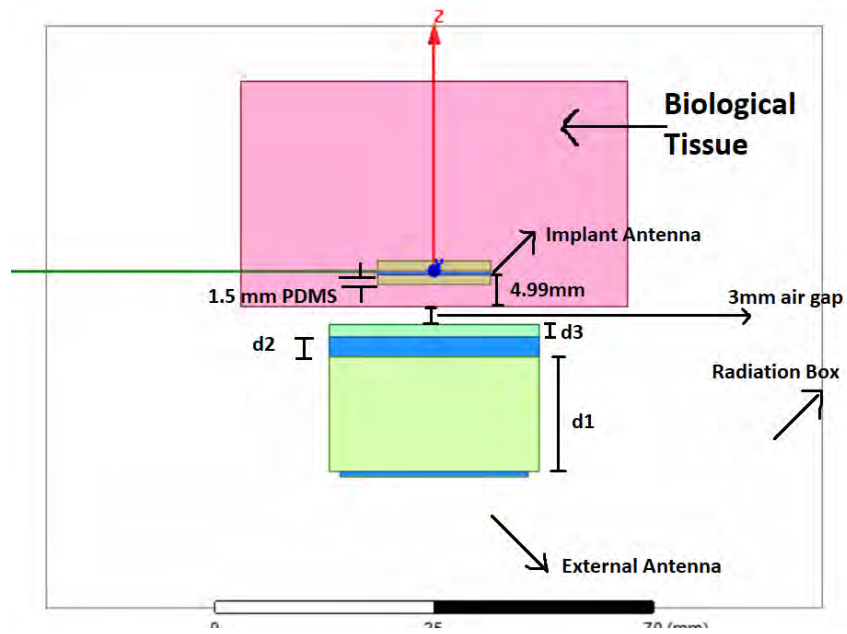
In CST studio, we have performed time domain analysis for the simulation, and there no such radiation boundary was needed. In CST, the simulation dimension was defined through the



(a)



(b)



(c)

Figure 4.2: Convenient 3D and sectional view of the whole proof of concept simulation design. Fig. 4.2a is the geometry in HFSS, Fig. 4.2b is the geometry in CST studio, and Fig. 4.2c is the sectional view with the defining dimensions.

boundary dimension which is a built-in design option. Convenient and sectional view of the final geometry is shown in Fig. 4.2.

4.2 Designing the Antenna

In this section we present the design of both the external and the implant antenna. As antenna substrates, we have chosen RogerRO4003 material, which has $\epsilon_r = 3.55$ and $\tan\delta = 0.0027$). The thickness of the substrates is chosen to be 0.762mm like [16].

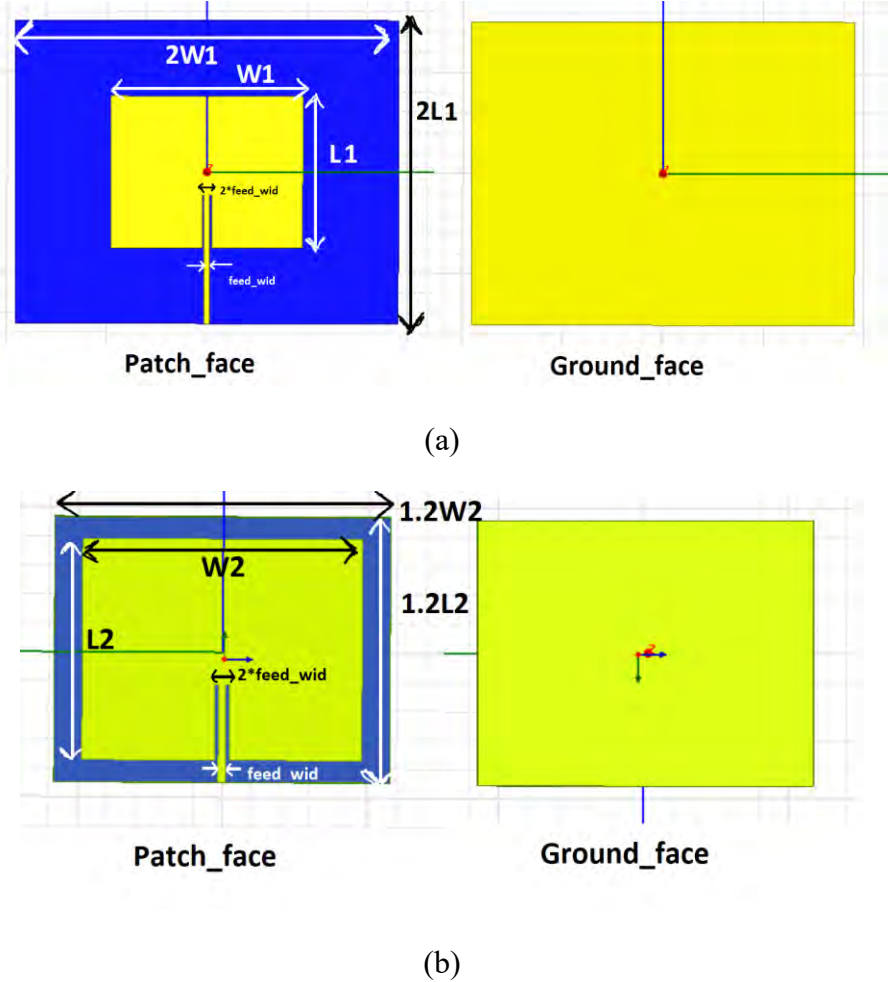


Figure 4.3: Geometry of the external (Fig. 4.3a) and the implant antenna (Fig. 4.3b) for the proof-of-concept design.

The patch and the ground surface are assumed to be PEC (Perfect Electric Conduction) sheets. For the implant antenna, the two surfaces are covered with PDMS material, to ensure biocompatibility and boost transmission. Views of the top and the bottom surfaces of both the antennas is presented in Fig.4.3.

Here,

$$L1 = 15.09mm, W1 = 19.12mm, L2 = 15.24mm, W2 = 19.31mm.$$

The antenna is fed with line feeding mechanism. For line feeds, lumped ports has been used in HFSS and discrete port has been used in CST studio. The length of the feed line (*feed_len*) is 5.24mm and the width of the feed (*feed_wid*) is chosen to be 0.5mm.

4.3 Designing the Superstrate and Metamaterial

For the superstrate, RogersRO4003 material has been used. The thickness of the superstrate has been optimized to 8.5 mm. Circular rings are printed on both sides of the superstrate. The gap between the external patch and the superstrate is filled with PDMS material.

The circular rings are printed like that presented in Fig. 3.4, with the following dimensions:

$$r = 2.1mm, c = 0.8mm, d = 0.2mm$$

Four unit cells are printed on both sides of the superstrate, which is shown to provide the optimum performance.

Referring to Fig.4.2c, we choose the distance between the external patch and the superstrate as $d1 = \frac{\lambda_{PDMS}}{2} = \frac{\lambda_{air}}{2\sqrt{\epsilon_{PDMS}}} \approx 18.675 mm$. The thickness of the superstrate $d2 =$

8.5mm. We also choose to shield the metamaterial conducting surface of the outer surface of the superstrate with a PDMS coating of thickness $d3 = 1.5mm$. Finally, we choose to incorporate a 3mm air gap from the outer face of the external engineering to the surface of the biological tissue.

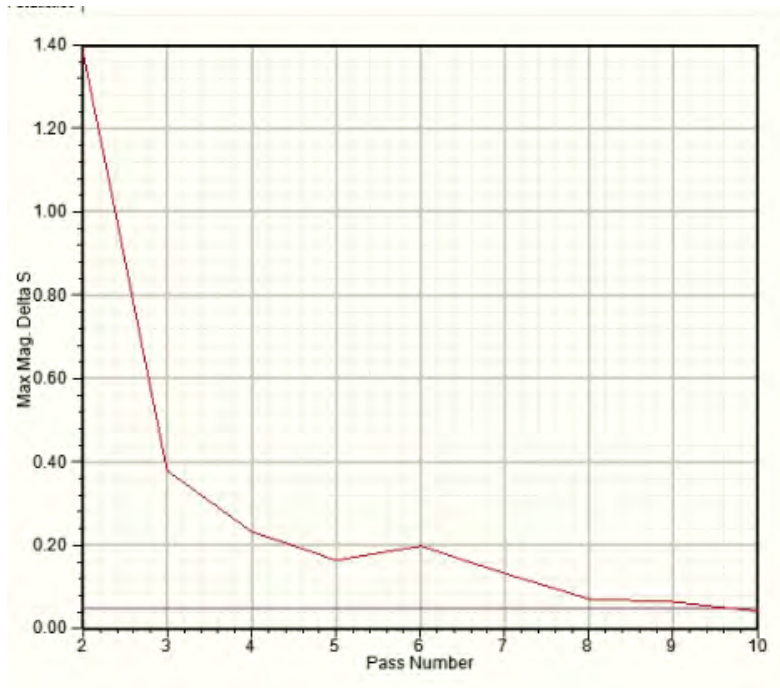


Figure 4.4: Convergence plot of the simulation with increasing adaptive pass

Since the design is a proof-of-concept design, it does not focus on any biosensing application, and depending on the application, many of the variables such as the air gap, or the coating in the external antenna can be removed and the antennas can be optimized accordingly.

4.4 Simulation

For the simulation, we choose a frequency range of 4.5 GHz to 5.1 GHz, therefore the frequency of interest (4.8GHz) is set as the central frequency. Adaptive meshing has been used for simulation, which auto updates the mesh according to a specified criterion. The convergence criterion (maximum ΔS) has been set to 0.02. The maximum number of adaptive pass has been set to 30, although it has been found that the desired convergence is obtained after 11-12 iterations.

The convergence plot (in HFSS) (See Fig. 4.4) shows a smooth convergence of the simulation, which is desired, and suggests that the simulation is set up properly.

4.5. Performance Analysis

4.5.1. Transmission Characteristics

The proof-of-concept design is simulated in both HFSS and CST studio. Transmission curve in the given frequency range is plotted and shown in Fig. 4.5.

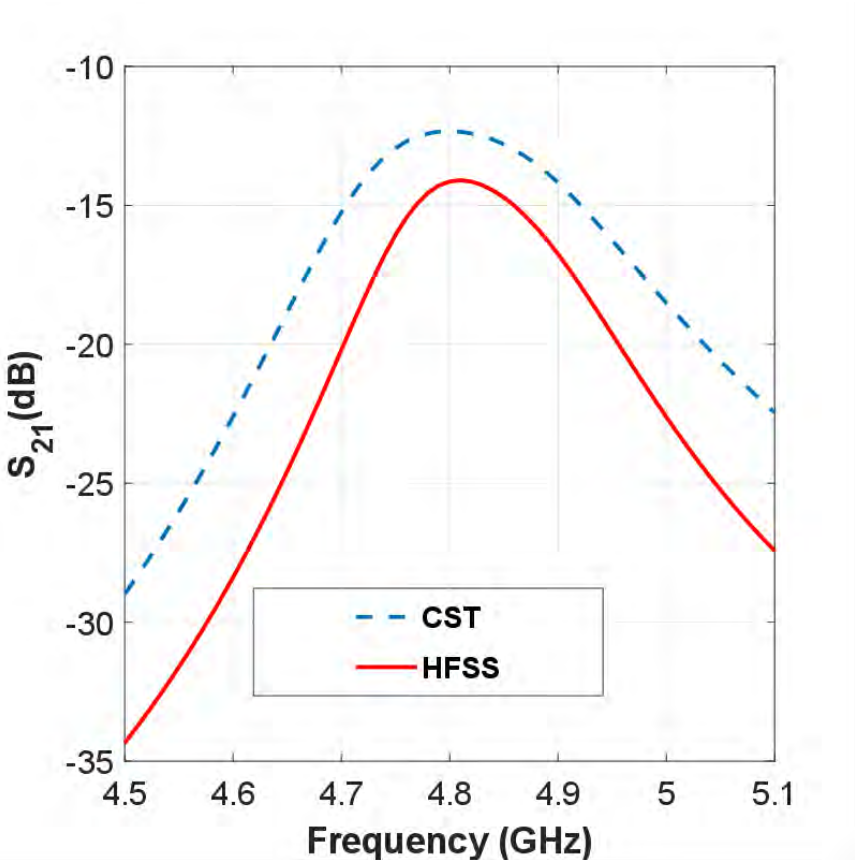


Figure 4.5: Transmission loss for the proof-of-concept design.

The transmission curve appears to be a very smooth curve with frequency, and the transmission performance is below -20 dB over a very large frequency range. For a possible neurosensing application, this comfortably meets the design criteria of system loss $< -25\text{ dB}$. The best transmission loss at the desired frequency of 4.8GHz is found to be -14.13 dB in the simulation in HFSS and -12.33 dB in the simulation in CST studio.

Comparing the performance of the proposed design with the baseline neuropotential system in [16], we see that in the work the transmission loss was 19dB (17 dB in simulations), and therefore the proposed design achieves a performance improvement of around 3dB .

TABLE 4.1: PERFORMANCE COMPARISON OF THE PROPOSED SYSTEM WITH EXISTING LITERATURE

Reference	Operating Frequency	Maximum S_{21}	External Antenna surface	Internal Antenna surface
[16]	$\sim 4.8\text{GHz}$	-19dB (-17dB in simulation)	145 mm diameter,	$15 \times 16\text{ mm}^2$
[40]	2.4 GHz	-22.5dB	$12 \times 12\text{ mm}^2$, $9 \times 10\text{ mm}^2$ etc.	Same as the external antenna
[41]	2.4GHz	-21.4dB	$24.9 \times 24.9\text{ mm}^2$	N/A
[42]	$\sim 4.8\text{GHz}$	-18.2 dB	$40 \times 40\text{ mm}^2$	$19.94 \times 29.17\text{ mm}^2$
[43]	400MHz (2.4GHz)	-33dB	$22 \times 23\text{ mm}^2$	N/A
[44]	400MHz	-24dB	$26.8 \times 28\text{ mm}^2$	N/A
Proposed Design	4.8GHz	-14.13dB in HFSS (-12.33dB in CST)	$30.9 \times 39.14\text{ mm}^2$	$18.288 \times 23.172\text{ mm}^2$

We also compare the geometry, bulk size, and the performance of the proposed design with some of the existing biopotential sensing works in Table 4.1.

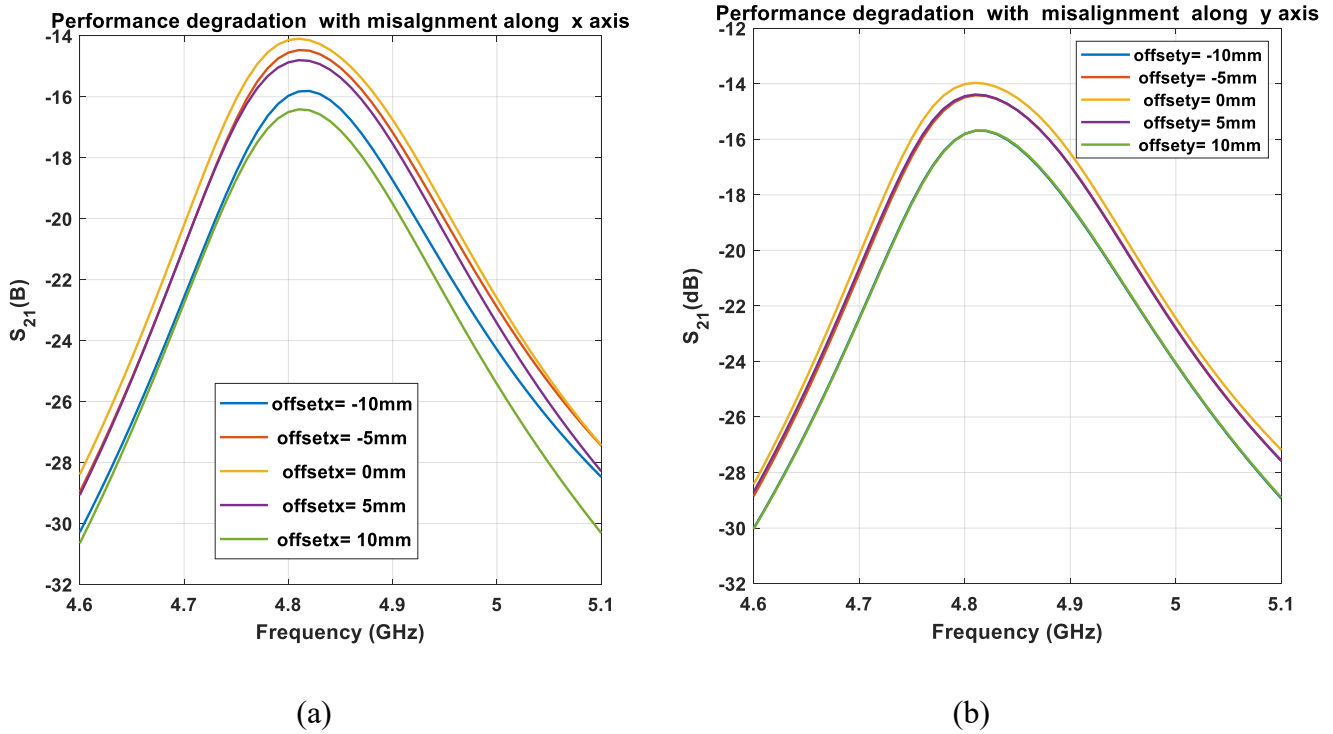


Figure 4.6: Performance degradation with misalignment along (a) x axis and (b) y axis

The transmission performance of the proposed design is better than all the reported works, while the dimension of the antennas are also comparable with the reported works.

One drawback of the proposed design is the bulk volume of the external antenna with the described engineering is slightly larger than those reported works. The external geometry is bulkier, and the layered structure could make the practical designs slightly more complex.

4.5.2 Misalignment Sensitivity

In this section we evaluate the performance of the proposed design in terms of misalignment of the external antenna from the central axis. Similar to the baseline study in [16], we offset the external antenna by a maximum distance of 10 mm from the central position, along both the x and y axis and observe the transmission degradation. The results are shown in Fig. 4.6.

From the misalignment chart, we can observe the following:

- There is a symmetry in the misalignment plot along the y axis, which is not present along x. The reason is, the antenna is line fed, and the location of the feedline made the

TABLE 4.2: EFFECT OF MISALIGNMENT IN THE TRANSMISSION PERFORMANCE OF THE PROPOSED DESIGN

Misalignment along x axis		Misalignment along y axis	
Distance (mm)	S_{21} degradation (dB)	Distance (mm)	S_{21} degradation (dB)
-10	1.83	-10	1.79
-5	0.42	-5	0.43
5	0.74	5	0.43
10	2.37	10	1.79

proposed design symmetric about the y axis. Whereas the presence of the feedline takes the symmetry away from the x axis. So, the result is expected.

- Even after the offset of the external antenna from the central position, the transmission performance is still very good, and the transmission loss is still above $-20dB$ quite comfortably.

In comparison, in the work in [16], we can see that the transmission loss degrades to below $-25dB$ for $10mm$ of antenna misalignment, which is actually lower than the desired requirement for the associated neuropotential sensing application.

In Fig. 2.3, we have showed the performance degradation with misalignment in [16], while in Table 4.2, we show the performance degradation in our proposed design for similar offset at the frequency of $4.8 GHz$.

Compared to the working the baseline literature, we see that the maximum loss due to misalignment is only $2.37 dB$, which is very low, and the design can maintain the performance requirement very easily.

4.6 Comparison with a Closely Coupled Antenna Pair System

Having discussed the possible merits of the proposed idea and the advantages of the proof-of-concept design over the existing literature, another comparison would also be illuminating. Here we present the transmission performance and the misalignment sensitivity of an antenna pair system where the external antenna is placed $3mm$ in front of the biological tissue, and the internal gap is devoid of any engineering. From the simulation of this system, we can show how much the proposed idea can enhance the lost transmission due to the increase of the antenna separation, and how much sensitive an equivalent near field coupled design would be in terms of misalignment.

4.6.1 Design of the Antenna System:

In this antenna system, the external antenna is placed directly $3mm$ in front of the biological tissue, the location of the implant antenna is kept the same as is the proposed design. However, now that the antenna pairs are close to each other, the resonant frequency altered slightly, and the dimensions of the two antennas were modified as follows:

$$L1 = 16.03 mm, W1 = 20.29 mm, L2 = 15.4mm, W2 = 19.5 mm$$

The dimensions of the feed lines and the coating thickness is kept the same as before. The materials which have been chosen in the proof-of-concept design is also kept the same.

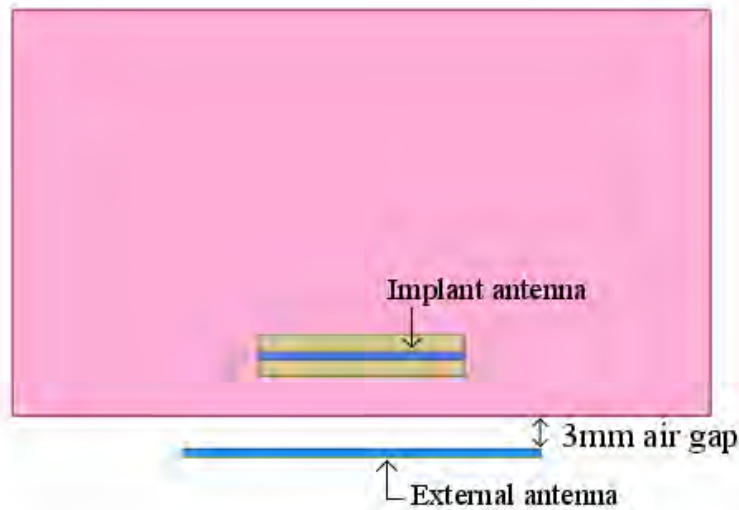


Figure 4.7: Sectional view of an antenna pair system without the engineering of the proposed concept.

A sectional view of the new antenna system is presented in Fig.4.7.

4.6.2 Transmission Analysis

For the new design, we again observe the transmission loss, with and without the presence of offset (See Fig.4.8), and from the results we take the following observations:

- The best transmission at the desired frequency of 4.8 GHz is found to be -13.43 dB , which is very similar to the performance of the proof-of-concept design. Therefore, the proof-of-concept design was able to recover the transmission performance atleast by the amount it was lost due to increasing the separation.

- The performance degradation due to the misalignment is much more severe compared to the proposed design. Furthermore, the resonant peak seems to shift with antenna offset along both x and y direction. Comparing with Fig 4.6, this system is much more unstable. Like Table 4.2, we present the transmission degradation with misalignment for the close antenna system in Table 4.3.

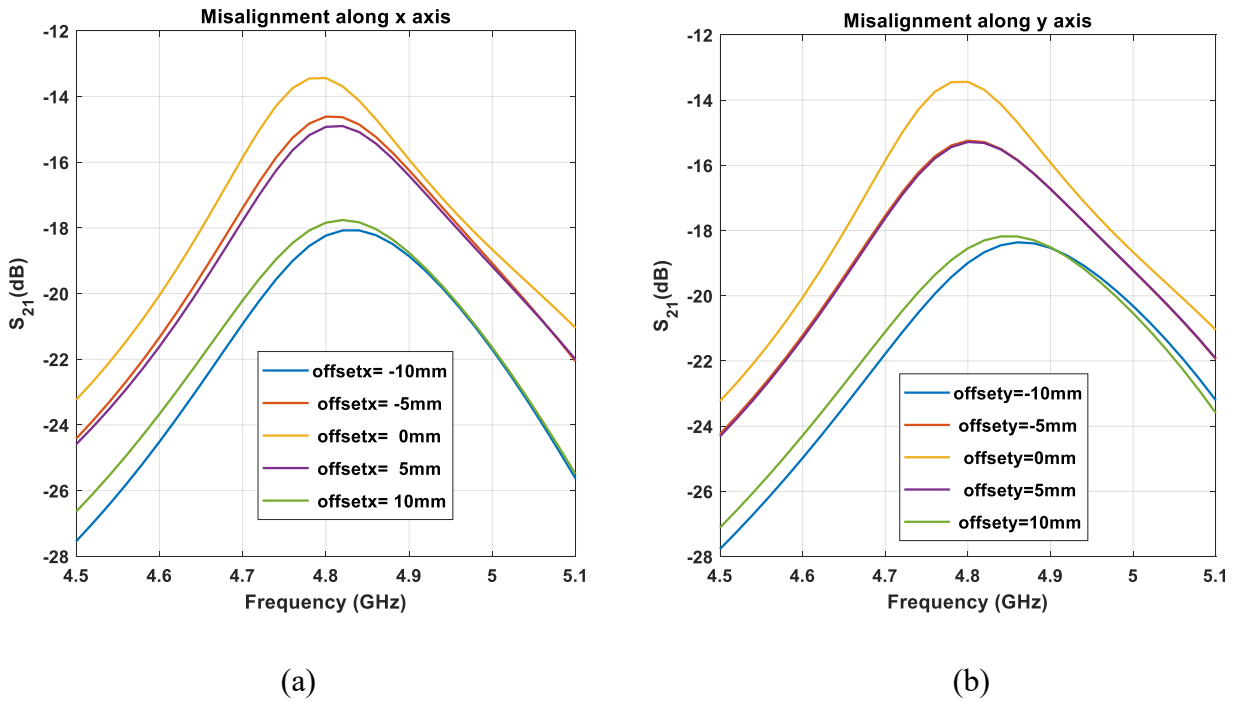


Figure 4.8: Performance degradation of the close antenna pair system with misalignment along (a) x axis and (b) y axis

Compared to the proposed design, here the maximum transmission loss is in the order of 6dB which is almost 4 dB lower than the proposed design and much more similar to the works of [16]. Therefore, this design is inferior in terms of performance to the proposed design.

The proposed design offers very high transmission performance as well as being very robust to the offset of the external antenna, which can be a very likely occurrence if the design concept is used on wearable passive sensing devices.

TABLE 4.3: EFFECT OF MISALIGNMENT IN THE TRANSMISSION PERFORMANCE OF THE CLOSELY SEPARATED ANTENNA PAIR

Misalignment along x axis		Misalignment along y axis	
Distance (mm)	S_{21} degradation (dB)	Distance (mm)	S_{21} degradation(dB)
-10	4.8	-10	5.56
-5	1.18	-5	1.85
5	1.49	5	1.85
10	4.41	10	5.11

4.7 Health Considerations:

While discussing the practical benefits of the proposed system for biosensing application, it is also important to address the specific absorption rate (SAR). SAR is a measurement of electromagnetic absorption inside a dispersive material in each volume (or mass). A higher amount of SAR indicates the material (biological tissue) is absorbing more radiation, which has long term negative consequences on the patient’s health.

For the calculation of SAR, we used the similar procedure used in [17]; we applied an excitation power of 6 dBm (0.0039625 Watts) to the carrier in the implant antenna, and calculated the SAR averaged over 1 g and 10 g of tissue. Averaging over 1 g of tissue, we measure an SAR value of 0.419 W/kg (See Fig. 4.9a), and for 10 g of tissue, we measure the SAR value to be 0.144 W/kg (See Fig. 4.9b).

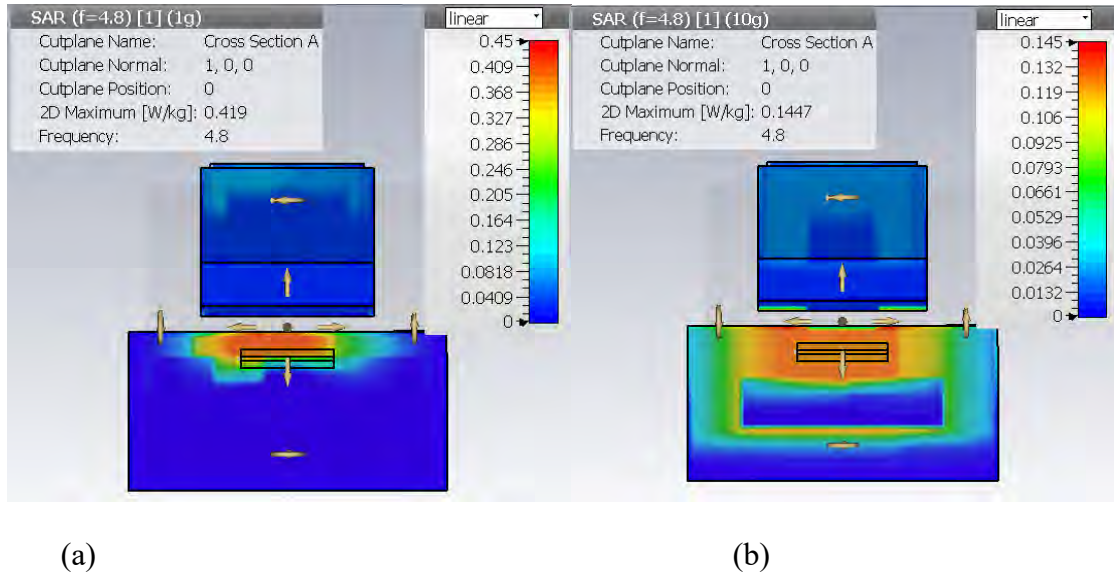


Figure 4.9: Cross sectional view of the SAR performance, averaged over 1 g (Fig. 4.9a) and 10 g (Fig. 4.9b) with input carrier power at 4.8 GHz set to 6 dBm (0.0039605 Watts)

The Federal Communication Commission (FCC)[45] requirement of maximum SAR for 1 g averaged biological tissue, under the given power of 6 dBm is 1.6 W/kg , and the International Commission on Non-Ionizing Radiation Protection (ICNIRP) [46] has defined the maximum averaged SAR for 10 g averaged tissue to be 2 W/Kg . Implementation of the proposed concept in biosensing has met both the requirements very efficiently.

4.8 Biosensing at a Different Frequency

While discussing the potential of the proposed method in passive biosensing system, we chose the frequency to be 4.8 GHz like the implant mixer frequency in [16,18], which is the second harmonic of the ISM band frequency of 2.4 GHz. However, as described in [6], each biological tissue has its own optimum frequency to facilitate a biopotential transmission.

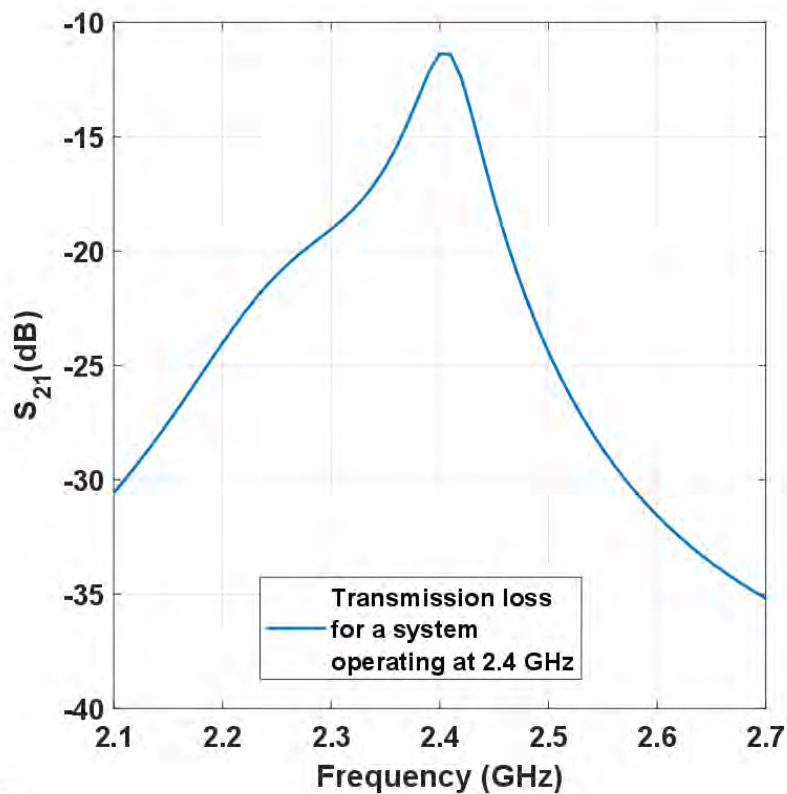


Figure 4.10: Transmission performance of an antenna pair system designed at 2.4 GHz (HFSS)

So, it is also of some importance to observe if the proposed idea can be implemented in any frequency of interest, with similar amount of performance. For that reason, we also present a biosensing system which operates at a different frequency (2.4 GHz). The geometry of the system is similar to Fig. 4.2, but the dimensions of each of the layers had to be changed accordingly. The dimensions of the antennas and the three layers in front of the external patch is given below:

$$L1 = L2 = 31.69\text{mm}, \quad W1 = W2 = 39.7\text{mm}$$

$$d1 = 37.35\text{ mm}, \quad d2 = 8.5\text{m}, \quad d3 = 1.5\text{mm}$$

The thickness of the air gap, the implant antenna depths and the coating thicknesses are kept same as before. For the new design, we report a maximum transmission gain of -11.375 dB at 2.4 GHz (See Fig.4.10). This high transmission performance ensures that the concept can be applied to any suitable frequency.

On the negative side, we see that the antenna dimensions are increased, which is expected as the operating frequency is lowered. The thickness of the gap material $d1$ has also increased by a factor of 2, which is due to maintain the $\frac{\lambda}{2}$ wavelength distance from the source patch to the superstrate. Therefore, at lower frequencies, the design dimensions will be larger and the whole system will be bulkier, which may not be ideal for implantable biosensing systems.

Chapter 5

A Passive Neurosensing System

Having discussed the potential of the proposed idea in biosensing applications with all practical considerations, we present a design of passive neurosensing system, and demonstrate a practical case of biosignals extraction, transmission, and reception through simulations.

5.1. System Design

where the biological tissue is a complex multilayered structure of skin, bone, grey matter, and white matter [17]. Each of the biological tissue is frequency dispersive with the dielectric curves shown in Fig. 5.1.

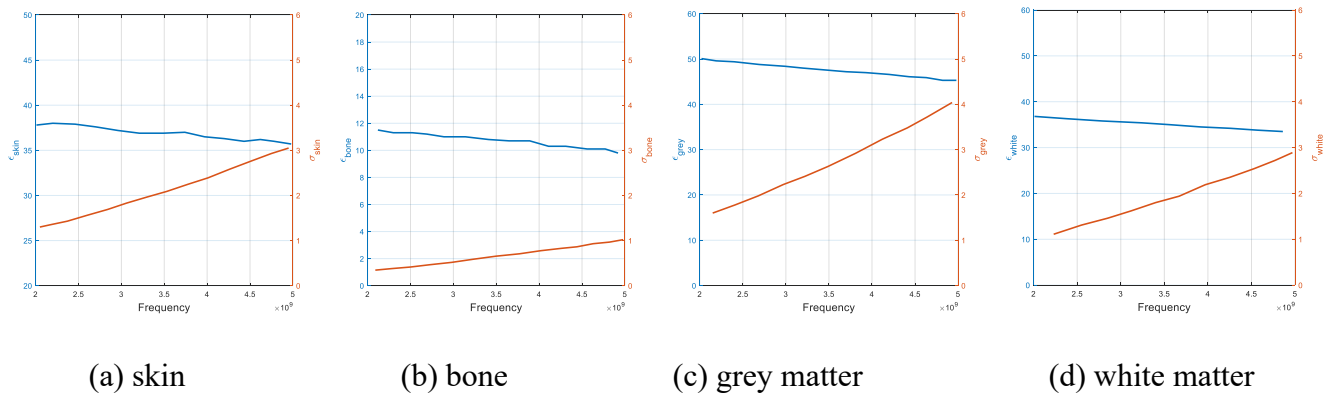


Figure 5.1: Frequency dependent dielectric constant (ϵ) and conductivity (σ) of the tissues to design the neurosensing system.

The arrangement of the neurosensing system is presented in Fig. 5.2a.

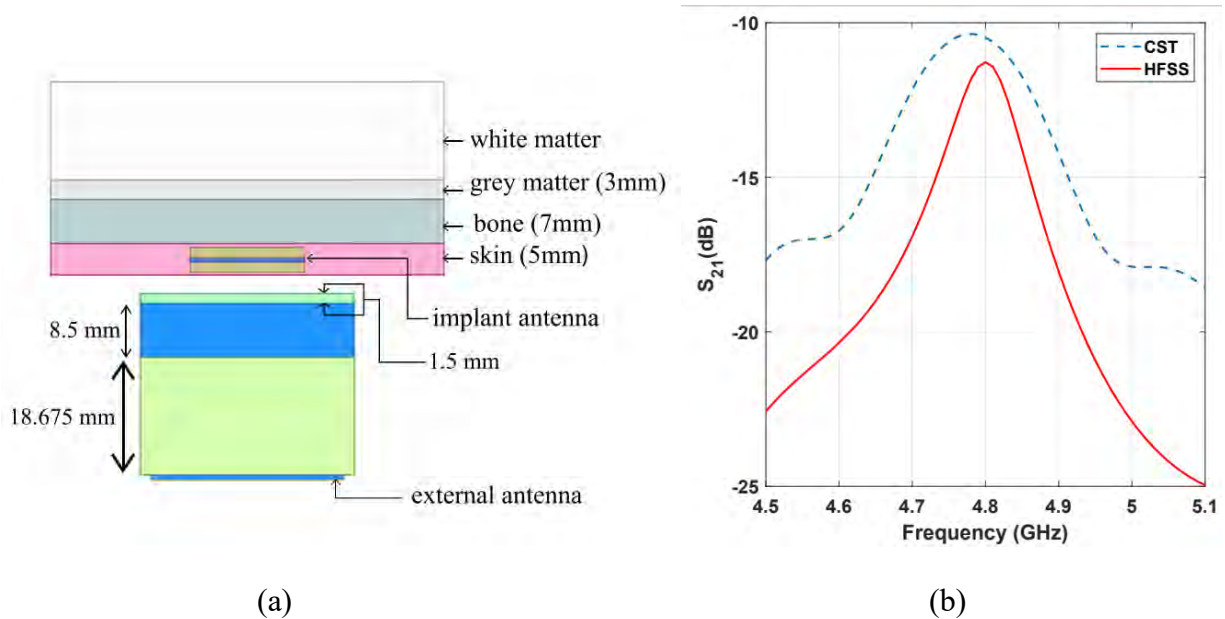


Figure 5.2: Design of a passive neurosensing system with optimized transmission curves.[47]

The implant antenna is buried 1mm inside the skin, and it is assumed the electrodes are buried inside to touch the grey matters to extract the necessary biopotentials. The design of the implant and the external antenna is similar to the ones discussed in section 4.2, with the following parameters:

$$L1 = L2 = 15.24 \text{ mm}, W1 = W2 = 19.31 \text{ mm}$$

5.2 Performance Analysis

5.2.1 Transmission Gain and Misalignment Sensitivity

For the above-mentioned design, the simulation results show a transmission loss of -11.27 dB in HFSS (-10.50 dB in CST studio) [47] (See Fig. 5.2b). The misalignment sensitivity analysis

showed that the maximum performance degradation is 2.41dB for 1cm of misalignment of the external antenna from the central position (See. Table 5.1).

TABLE 5.1: EFFECT OF MISALIGNMENT IN THE TRANSMISSION PERFORMANCE OF THE NEUROPOTENTIAL SENSING SYSTEM

Misalignment along x axis		Misalignment along y axis	
Distance (mm)	S_{21} degradation (dB)	Distance (mm)	S_{21} degradation(dB)
-10	2.41	-10	1.11
-5	0.67	-5	0.14
5	0.62	5	0.14
10	2.33	10	1.11

5.2.2 SAR Calculation

For the neurosensing system, similar SAR analysis has shown that an average over 1g of tissue gives a specific absorption of 0.1246 W/kg , and an average over 10g of tissue gives a specific absorption of 0.0587 W/kg . Each absorption amounts comfortably satisfy the safety regulations, although suggest a slightly higher absorption in comparison to the neurosensing system in [17].

5.3 System Level Modeling of Neopotential Extraction

5.3.1 System Overview

In this section we present the neurosensing antenna design to emulate a full neopotential extraction system. We follow the scheme similar to[16]. We choose a neurosignal which has a frequency of 1KHz , but instead of choosing signal power of -70 dBm , we choose the input signal has the minimum neurosignal amplitude of -82 dBm (50Vpp). We have added a gaussian noise with the source signal to model the extraction impairments, and the noise has an assumed SNR of 10. Throughout the analysis, we have assumed a 50 ohm source impedance.

The signal is mixed with a carrier of frequency 4.8 GHz , which is modelled as a suppressed carrier amplitude modulation. The work in [16] assumed a maximum mixer conversion loss of 25 dB , which happens during the modulation process, and we have coded and incorporated the loss by scaling the modulated signal by similar amount.

The modulated signal is passed through the antenna pair system which has been designed in section 5.1. We model the antenna as a passive circuit element, which has a frequency dependent gain. The S parameters are extracted from the simulation file in HFSS in touchstone (.s2p) format and applied on the passive element to form the antenna system.

In the receiver block, the signal is demodulated with the same carrier signal, which is coherent demodulation, and later passed through a low pass filter to extract the fundamental frequency of the source signal. In the simulation, we have not chosen to apply any signal amplification, which can be placed arbitrarily in between any point from the modulation system to the demodulation point.

The whole system is simulated using MATLAB, and the code is available in Appendix A.

5.3.2 Resolution of the Spectrum

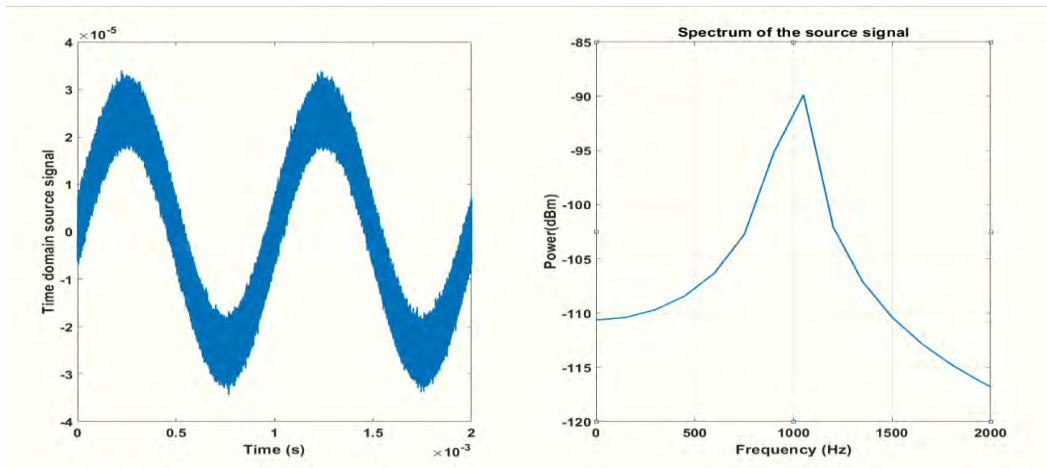
To obtain the frequency spectrum of a low frequency signal modulated with a very large carrier, we face the problem of spectral resolution in the frequency domain plots. We know that the signals must be sampled at least twice the maximum used frequency (Here, the carrier frequency). For a 4.8 GHz carrier, therefore, we can choose a sampling frequency of $F_s \approx$

$2.5 \times 4.8 \text{ GHz}$, translating to a sample time of $\approx 10^{-10}$ seconds. The spectral resolution, which is also defined as the frequency interval in the power spectrum is defined as [48]:

$$\text{resolution} \approx \frac{F_s}{N}$$

Here N is the number of samples in the window, which has been used to estimate the spectrum of the time sampled signal. The resolution decreases with increased number of samples N . The maximum possible choice of N to determine the spectrum of a finite signal is to have the same size as the source signal. And therefore, the time domain signal therefore must also have N discrete sequences for proper frequency estimation.

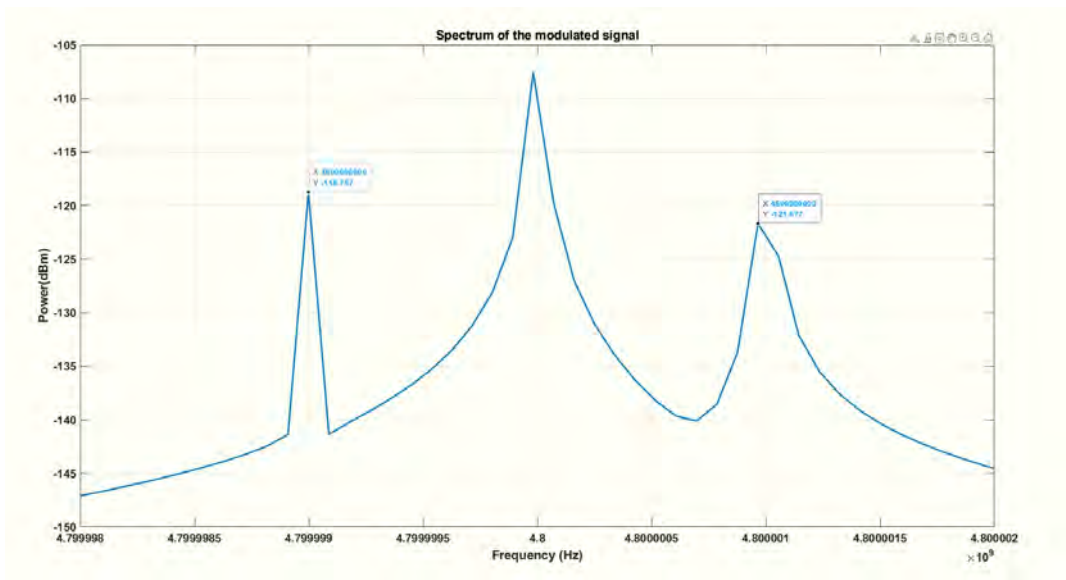
To visualize the spectrum of a 1 KHz source signal, the resolution must be much less than the signal frequency. If we choose a resolution of 100 Hz , the above equation suggests that the number of data points is $N = 10^9$ which is an abnormally large amount of data. For low RAM machines, this means the system may run out of memory, and therefore an arbitrarily high resolution of the source signal is not possible. We have chosen $N = 2^{27}$ sample (See Appendix-A), with a resolution of 89.3 Hz , which can be simulated using a 16 GB RAM machine.



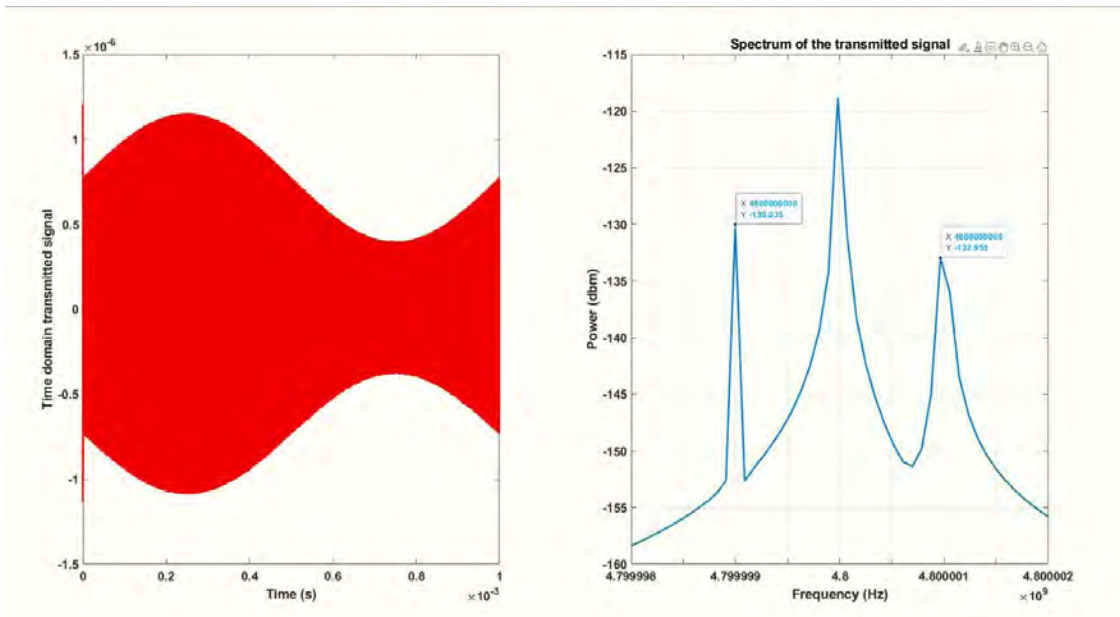
(a) The time domain source signal and its frequency spectrum

5.3.3 Simulation Results

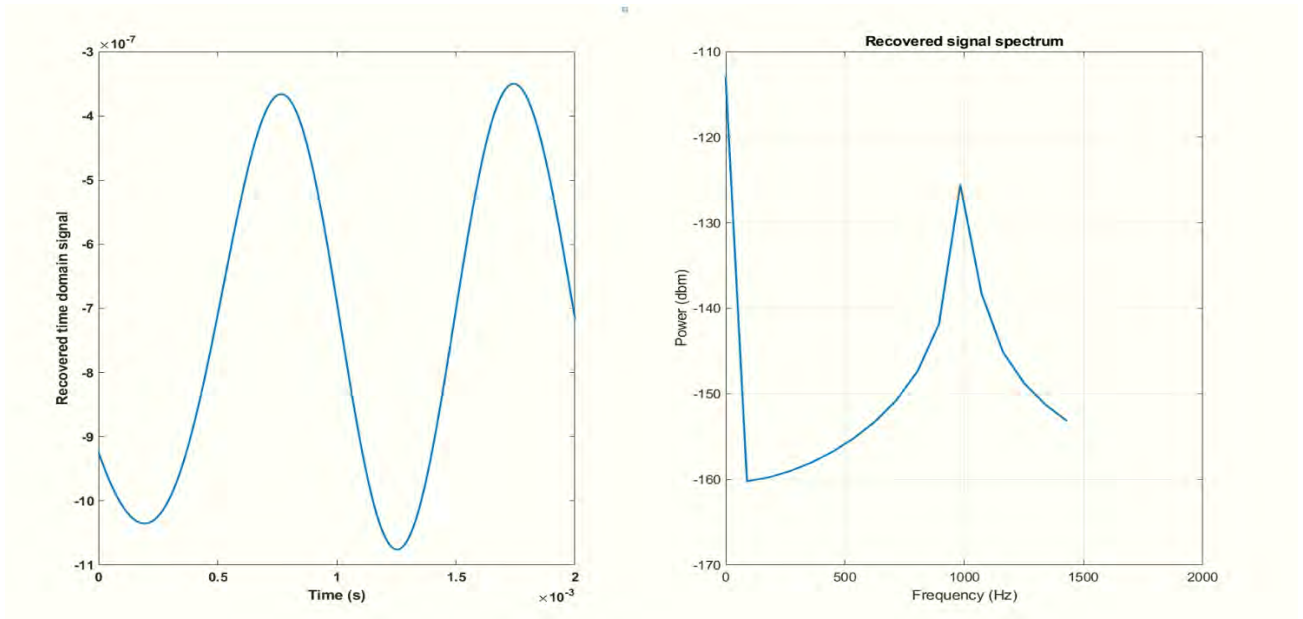
In this section, we present the signal transition in each step of the signal extraction process. (See Fig.5.3)



(b) Spectrum of the Modulated Signal



(c) Time domain and spectral representation of the received signal



(d) Recovered signal at the receiver after demodulation and low pass filtering

Figure 5.3: Extraction of weak neuropotentials with the proposed antenna system.

In Fig. 5.3a, we see the input source signal, which is slightly corrupted by gaussian noise. The input signal is passed through a mixer, and the source spectrum amplitude reduces from -88 dB to $\approx -123 \text{ dB}$ (See Fig. 5.3b). After transmitting the modulated signal through the modelled antenna system, the magnitude further degraded and we receive a $\approx -135 \text{ dB}$ signal (See Fig. 5.3c), which agrees to the transmission loss of the antenna. Finally, after demodulation and low pass filtering, we see that the higher frequency components have been removed and the original signal has been recovered (Fig. 5.3d), however there is some small difference between two adjacent peaks in the received signal.

Chapter 6

Conclusion

A new method of transmission enhancement and misalignment mitigation between internal and external antenna pair for biopotential sensing is proposed in this paper. A fullwave simulation of a typical neuropotential system is carried out, taking into account the realistic permittivity and conductivity of biological tissues, along with proper modeling of the antenna pair. Exploiting the theory of Fabry-Perot resonators and metamaterials, the proposed technique achieves a very high transmission gain of around -11 dB. The design also appears to be very stable under possible misalignment of the antenna pairs and meets the safety requirements.

6.1 Major Contributions

The whole investigation of transmission enhancement is completely novel, and therefore provides a significant amount of information to the scientific community. The merge of the Fabry Perot concept cavity with a new proposal has resulted in a very attractive method of biosensing extraction, which can have significant impact in future. The investigation of transmission enhancement in chapter 3, suggest that the proposed idea is also applicable in the free space far field communication.

6.2 Future Research Directions

While the studies show very promising results and is consistent with the theoretical expectations and intuition, the feasibility of the proposed method needs real time testing, which requires design and implementation in various laboratory scales. A good experimental prototype is necessary to comment on the practicality of the proposed concept.

Another important observation to take note is that, in the thesis we have not put much attention to the antenna geometries and the complications. Depending on the specific application, it may be possible to design complex antennas with more radiation efficiency along the transmission direction. The design criteria and use of more complex antenna geometries with the proposed concept is required and is a part of further research.

References

- [1] Schomer, D.L. and Da Silva, F.L.,. Niedermeyer's electroencephalography: basic principles, clinical applications, and related fields. Lippincott Williams & Wilkins. 2012
- [2] Kamen, G. and Kinesiology, E., 2004. Research methods in biomechanics. Champaign, IL, *Human Kinetics Publ.* 2004
- [3] Lilly, L.S.. Pathophysiology of heart disease: a collaborative project of medical students and faculty. Lippincott Williams & Wilkins,2012
- [4] Bulling, A. et al.: Eye Movement Analysis for Activity Recognition Using Electrooculography, *IEEE Transactions on Pattern Analysis and Machine Intelligence*, in press.
- [5] de Melo, J. L., Querido, F., Paulino, N., & Goes, J. A 0.4-V 410-nW opamp-less continuous-time $\Sigma\Delta$ modulator for biomedical applications. In *2014 IEEE International Symposium on Circuits and Systems (ISCAS)* (pp. 1340-1343). IEEE. 2014.
- [6] Poon, A. S., O'Driscoll, S., & Meng, T. H.. Optimal frequency for wireless power transmission into dispersive tissue. *IEEE Transactions on Antennas and Propagation*, 58(5), 1739-1750. 2010
- [7] H. Ling, S.-W. Lee, and W. Gee, "Frequency optimization of focused microwave hyperthermia applicators," *Proc. IEEE*, vol. 72, no. 2, pp. 224–225, 1984
- [8] K.D. Wise, "Microelectrodes, microelectronics, and implantable neural microsystems," *Proc. IEEE*, vol. 96, no. 7, pp. 1184–1202, 2008.
- [9] E. Moradi, T. Bjorninen, L. Sydanheimo, J. M. Carmena, J. M. Rabaey, and L. Ukkonen, "Measurement of wireless link for brain-machine interface systems using human-head equivalent liquid," *IEEE Antennas Wireless Propag. Lett.*, vol. 12, pp. 1307–1310, 2013.
- [10] E. Moradi, K. Koski, T. Bjorninen, L. Sydanheimo, J. M. Rabaey, J. M. Carmena, Y. Rahmat-Samii, and L. Ukkonen, "Miniature implantable and wearable on-body antennas:

Towards the new era of wireless body-centric systems,” *IEEE Antennas Propag. Mag.*, vol. 56, no. 1, pp. 271–291, 2014.

[11] S. Kim, P. Thathireddy, R.A. Normann, and F. Solzbacher, “Thermal impact of an active 3-D microelectrode array implanted in the brain,” *IEEE Trans. Neural Syst. Rehab. Eng.*, vol. 15, pp. 493–501, 2007.

[12] M. Yin, D.A. Borton, J. Komar, N. Agha, Y. Lu, H. Li, J. Laurens, Y. Lang, Q. Li, C. Bull, L. Larson, D. Rosler, E. Bezar, G. Courtine, A.V. Nurmikko, “Wireless neurosensor for full-spectrum electrophysiology recordings during free behavior,” *Neuron.*, vol. 84, pp. 1-13, 2014.

[13] G. Schalk and E. C. Leuthardt, “Brain-computer interfaces using electrocorticographic signals,” *IEEE Rev. Biomed. Eng.*, vol. 4, pp. 140–154, 2011.

[14] H. N. Schwerdt, W. Xu, S. Shekhar, A. Abbaspour-Tamijani, B. C. Towe, F. A. Miranda, and J. Chae, “A fully passive wireless microsystem for recording of neuropotentials using RF backscattering methods,” *J. Microelectromech. Syst.*, vol. 20, pp. 1119–1130, 2011.

[15] H. N. Schwerdt, F. A. Miranda, and J. Chae, “A fully passive wireless backscattering neurorecording microsystem embedded in dispersive human-head phantom medium,” *IEEE Electron. Device Lett.*, vol. 33, no. 6, pp. 908–910, 2012.

[16] Lee, C. W., Kiourti, A., Chae, J., & Volakis, J. L. A high-sensitivity fully passive neurosensing system for wireless brain signal monitoring. *IEEE Transactions on Microwave Theory and Techniques*, 63(6), 2060-2068. 2015

[17] Lee, C. W., Kiourti, A., & Volakis, J. L.. Miniaturized fully passive brain implant for wireless neuropotential acquisition. *IEEE Antennas and Wireless Propagation Letters*, 16, 645-648. 2016

[18] Kiourti, A., Lee, C. W., Chae, J., & Volakis, J. L. A wireless fully passive neural recording device for unobtrusive neuropotential monitoring. *IEEE Transactions on Biomedical Engineering*, 63(1), 131-137. 2015

[19] Balanis, C.A.. *Advanced engineering electromagnetics*. John Wiley & Sons.2012.

[20] Veselago, V. G.. Electrodynamics of substances with simultaneously negative and. *Usp. Fiz. Nauk*, 92, 517. 1967

- [21] Maier, S.A., 2007. "Plasmonics: fundamentals and applications". Springer Science & Business Media.
- [22] Pendry, J. B., Holden, A. J., Stewart, W. J., & Youngs, I. Extremely low frequency plasmons in metallic mesostructures. *Physical review letters*, 76(25), 4773. 1996
- [23] Pendry, J.B., Holden, A.J., Robbins, D.J. and Stewart, W.J. Low frequency plasmons in thin-wire structures. *Journal of Physics: Condensed Matter*, 10(22), p.4785.1998
- [24] Pendry, J. B., Holden, A. J., Robbins, D. J., & Stewart, W. J. Magnetism from conductors and enhanced nonlinear phenomena. *IEEE transactions on microwave theory and techniques*, 47(11), 2075-2084. 1999.
- [25] Smith, D. R., Padilla, W. J., Vier, D. C., Nemat-Nasser, S. C., & Schultz, S. Composite medium with simultaneously negative permeability and permittivity. *Physical review letters*, 84(18), 4184. 2000
- [26] Enoch, Stefan, Gérard Tayeb, Pierre Sabouroux, Nicolas Guérin, and Patrick Vincent. "A metamaterial for directive emission." *Physical Review Letters* 89, no. 21 (2002): 213902.
- [27] Trentini, G. V.. Partially reflecting sheet arrays. *IRE Transactions on antennas and propagation*, 4(4), 666-671. 1956
- [28] Pendry, J.B.. Negative refraction makes a perfect lens. *Physical review letters*, 85(18), p.3966., 2000
- [29] Ziolkowski, R. W., & Heyman, E.. Wave propagation in media having negative permittivity and permeability. *Physical review E*, 64(5), 056625, 2001.
- [30] Burokur, S. N., Latrach, M., & Toutain, S.. Theoretical investigation of a circular patch antenna in the presence of a left-handed medium. *IEEE antennas and Wireless propagation letters*, 4, 183-186. 2005.
- [31] Majid, H. A., Abd Rahim, M. K., & Masri, T.. Microstrip antenna's gain enhancement using left-handed metamaterial structure. *Progress in Electromagnetics Research*, 8, 235-247. 2009
- [32] Wu, B. I., Wang, W., Pacheco, J., Chen, X., Grzegorzcyk, T. M., & Kong, J. A. A study of using metamaterials as antenna substrate to enhance gain. *Progress in electromagnetics research*, 51, 295-328. 2005

- [33] Feresidis, A. P., & Vardaxoglou, J. C.. High gain planar antenna using optimised partially reflective surfaces. *IEE Proceedings-Microwaves, Antennas and Propagation*, 148(6), 345-350. 2001.
- [34] Wang, S., Feresidis, A. P., Goussetis, G., & Vardaxoglou, J. C.. High-gain subwavelength resonant cavity antennas based on metamaterial ground planes. *IEE Proceedings-Microwaves, Antennas and Propagation*, 153(1), 1-6. 2006.
- [35] Kaymaram, F., & Shafai, L.. Enhancement of microstrip antenna directivity using double-superstrate configurations. *Canadian Journal of Electrical and Computer Engineering*, 32(2), 77-82. 2007.
- [36] Foroozesh, A., & Shafai, L.. Investigation into the effects of the reflection phase characteristics of highly-reflective superstrates on resonant cavity antennas. *IEEE transactions on antennas and propagation*, 58(10), 3392-3396. 2010.
- [37] Liu, H., Lei, S., Shi, X., & Li, L.. Study of antenna superstrates using metamaterials for directivity enhancement based on Fabry-Perot resonant cavity. *International Journal of Antennas and Propagation*, 2013.
- [38]. Gabriel, S., Lau, R. W., & Gabriel, C. The dielectric properties of biological tissues: II. Measurements in the frequency range 10 Hz to 20 GHz. *Physics in medicine & biology*, 41(11), 2251. 1996
- [39] Merli, F., Fuchs, B., Mosig, J. R., & Skrivervik, A. K. The effect of insulating layers on the performance of implanted antennas. *IEEE Transactions on Antennas and propagation*, 59(1), 21-31. 2010.
- [40] Bahrami, H., Mirbozorgi, S. A., Ameli, R., Rusch, L. A., & Gosselin, B.. Flexible, polarization-diverse UWB antennas for implantable neural recording systems. *IEEE transactions on biomedical circuits and systems*, 10(1), 38-48. 2015
- [41] Blauert, J., & Kiourti, A.. Theoretical modeling and design guidelines for a new class of wearable bio-matched antennas. *IEEE Transactions on Antennas and Propagation*, 68(3), 2040-2049. 2019.

- [42] Chen, Wei-Chuan, et al. "A multi-channel passive brain implant for wireless neuropotential monitoring." *IEEE Journal of Electromagnetics, RF and Microwaves in Medicine and Biology* 2.4: 262-269. 2018
- [43] Liu, Y., Chen, Y., Lin, H., & Juwono, F. H.. A novel differentially fed compact dual-band implantable antenna for biotelemetry applications. *IEEE Antennas and Wireless Propagation Letters*, 15, 1791-1794. 2016.
- [44] Xu, Li-Jie, et al. "A dual-band on-body repeater antenna for body sensor network." *IEEE Antennas and Wireless Propagation Letters* 15 .1649-1652. 2016.
- [45] Federal Communications Commission, Report and order: Guidelines for evaluating the environmental effects of radiofrequency radiation. *FCC 96-326*. 1996.
- [46] International Commission on Non-Ionizing Radiation Protection. Guidelines for limiting exposure to time-varying electric, magnetic, and electromagnetic fields (up to 300 GHz). *Health physics*, 74(4), pp.494-522. 1998.
- [47] Islam, M.S., Kiourti, A. and Islam, M.A.,. A Novel Method of Transmission Enhancement and Misalignment Mitigation between Implant and External Antennas for Efficient Biopotential Sensing. *Sensors*, 21(20), p.6730. 2021
- [48] Hayes, Monson H. "Statistical digital signal processing and modeling". 2009.

Appendix -A

Code for Simulation of the Neurosensing System

Main function:

```
clc
clear, close all

%% initalizations
fc= 4.8e9; % the carrier frequency
fs = 2.5*fc; % the sampling rate
ts= 1/fs; % the sampling time

fm= 1e3; % the message signal frequency
tm= 1/fm ; % the time interval of the received signals, for plotting
N= 2^27; % number of fft points, increasing the resolution further
consumes all the memory

t = ts: ts: N*ts;
resolution= fs/N
length(t);
freq = -fs/2:resolution:fs/2-resolution;
z= 50; % the reference impedance.

%% Generation of the input signal
```

```

sourcedBm= -82; % the source neurosignal with a peak to peak voltage
of 50 u V

a= dbm2v (sourcedBm, 50);

m1= a* sin( 2* pi* fm * t);

%adding white noise with given snr

m= awgn(m1,20,'measured');

m_dft = fftshift(fft(m,N))/N;

figure(1)
subplot(121),plot(t, m, 'linewidth', 2)
xlim ([0 tm])
xlabel('Time (s)')
ylabel('Time domain source signal')
subplot(122), plot(freq,v2dbm(m_dft,50), 'linewidth', 2)
xlim ([0 2*fm])
grid on
title('Spectrum of the source signal','fontsize', 14)
xlabel('Frequency (Hz)','fontsize', 14)
ylabel('Power(dBm)','fontsize', 14)

%% clear variables to save memory

clear m1 m_dft;

```

```

%% modulate with the carrier

carrierdBm= 6; % the carrier neurosignal with a peak to peak voltage
of 50 u V

ac= dbm2v (carrierdBm, 50)

c= ac* sin ( 2*pi* fc* t);

% c_dft = fftshift(fft(c,N))/N;

%% modulation and the spectrum of the modulated signal

modulated= ammod(m+2*a, fc, fs, 0); % mixing or suppressed carrier
modulation

% adding mixing conversion loss of 25dB

mixing_loss_dB= 25;

mixing_loss = 10^(mixing_loss_dB/20);

modulated= modulated/mixing_loss;

mod_dft = fftshift(fft(modulated,N))/N;

figure(2)

plot(freq,v2dbm(mod_dft,z), 'linewidth', 2)

grid on

title('Spectrum of the modulated signal')

xlabel('Frequency (Hz)')

ylabel('Power(dBm)')

xlim([ fc-2*fm fc+2*fm])

```

```

%% transmission of the modulated signal through a S parameter antenna
channel

% creation of a rf data network to simulate the amplifier, and
extracting

% the s parameters

antenna=read(rfckt.amplifier,
'F:\matlabandsimulink\neurosignals.s2p');

temp = analyze (antenna, [0:resolution: fs/2]);

S= temp.AnalyzedResult.S_Parameters;

S21= transpose(squeeze(S(2,1,:)));

% S21= abs([fliplr((S21(2:end))) S21(1:end-1)]);

S21= [fliplr(conj(S21(2:end))) S21(1:end-1)];

% S21= abs(S21);

figure(3)

plot(freq, 20*log10(abs(S21)), 'linewidth', 2)

grid on

xlabel('Frequency (Hz)')

ylabel('S_{21} (dB)')

title ('Retreived S parameter from the neurosensor (HFSS)')

xlim([4.5 5.1]*1e9)

%% clear variables to save memory

clear temp S

```



```

%% memory allocation problem, so the transfer characteristics needs to
be included in partition

trans_dft=[];

blocklen= 2^22;

for i= 1: length(freq)/blocklen

trans_dft= [trans_dftmod_dft((i-1)*blocklen+1:i*blocklen).* S21((i-
1)*blocklen+1:i*blocklen)];

    length(trans_dft)

    (i-1)*blocklen+1

i*blocklen

end

%% recover the transmitted time domain signal

transmitted = N*ifft(fftshift(trans_dft));

transmitted= real(transmitted);

figure (4)

subplot(121), plot (t, transmitted, 'r', 'linewidth',2)

xlabel('Time (s)','fontsize', 14)

ylabel('Time domain transmitted signal', 'fontsize', 14)

xlim([0, tm])

subplot(122),plot(freq,(v2dbm(trans_dft,z)), 'linewidth',2)

grid on

title('Spectrum of the transmitted signal')

xlabel('Frequency (Hz)')

ylabel('Power (dbm)')

xlim([ fc-2*fm  fc+2*fm])

```

```

%% demodulate the transmitted signal with the carrier to extract
output

demodulated= amdemod(transmitted , fc, fs, 0); % the input signal is
transmitted, needs to change later

% demodulated= (transmitted).*c; % cohererent demodulation technique
demod_dft = fftshift(fft(demodulated))/N;

figure(5)

subplot(121),plot(t, demodulated, 'linewidth', 2)

xlim ([0 tm])

xlabel ('Time (s)');

ylabel('demodulated signal')

subplot(122),plot(freq,v2dbm(demod_dft,z), 'linewidth', 2)

xlim ([0 2*fm])

grid on

title('Demodulation spectrum')

xlabel('Frequency (Hz)')

ylabel('Power (dbm)')

%% passing the demodulated signal through an ideal low pass fiter,
addressing memory concern

cutoff = 1.5*fm

temp= fs/ cutoff;

filter= zeros (1, length(freq)/2);

```

```

filter(1:ceil(N/temp))=1;
filter= [fliplr(filter(1:end)) filter];
rec_dft=[];
for i= 1: length(freq)/blocklen
    rec_dft=          [rec_dftdemod_dft((i-1)*blocklen+1:i*blocklen).*
    filter((i-1)*blocklen+1:i*blocklen)];
    (i-1)*blocklen+1
i*blocklen
end
recovered = N*ifft(fftshift(rec_dft)); %creating the recovered signal
in time domain
recovered= real(recovered);

%%
figure(6)
subplot(121),plot(t, recovered, 'linewidth', 2)
xlim ([0 2*tm])
xlabel ('Time (s)');
ylabel('Recovered time domain signal')
subplot (122), plot(freq,v2dbm(rec_dft,z), 'linewidth', 2)
xlim ([0 2*fm])
grid on
title('Recovered signal spectrum')
xlabel('Frequency (Hz)')
ylabel('Power (dbm)')
% plot(t,recovered);
% title('Recovered signal');

```

Other functions:

```
function y= dbm2v (dbm, z)
    p= 10.^(dbm/10) * 1e-3; % conversion to wattes
    y = sqrt(2*p*z);
end
```

```
function y= v2dbm (v,z)
    y= 10*log10(abs(v.^2/ (2*z)))+30;
end
```